



COMPRESSIVE COHERENT STRUCTURES AT ION SCALES IN THE SLOW SOLAR WIND

D. PERRONE^{1,2}, O. ALEXANDROVA¹, A. MANGENEY¹, M. MAKSIMOVIC¹, C. LACOMBE¹, V. RAKOTO¹,
J. C. KASPER³, AND D. JOVANOVIĆ⁴

¹ LESIA, Observatoire de Paris, PSL Research University, CNRS, Sorbonne Universités, UPMC Univ. Paris 06, Univ. Paris Diderot, Sorbonne Paris Cité, France

² European Space Agency, Science and Robotic Exploration Directorate, ESAC, Madrid, Spain

³ University of Michigan, Ann Arbor, MI, USA

⁴ Institute of Physics, University Belgrade, Belgrade, Serbia

Received 2015 November 26; revised 2016 April 29; accepted 2016 May 1; published 2016 July 29

ABSTRACT

We present a study of magnetic field fluctuations in a slow solar wind stream, close to ion scales, where an increase of the level of magnetic compressibility is observed. Here, the nature of these compressive fluctuations is found to be characterized by coherent structures. Although previous studies have shown that current sheets can be considered the principal cause of intermittency at ion scales, here we show for the first time that, in the case of the slow solar wind, a large variety of coherent structures contributes to intermittency at proton scales, and current sheets are not the most common. Specifically, we find compressive ($\delta b_{\parallel} \gg \delta b_{\perp}$), linearly polarized structures in the form of magnetic holes, solitons, and shock waves. Examples of Alfvénic structures ($\delta b_{\perp} > \delta b_{\parallel}$) are identified as current sheets and vortex-like structures. Some of these vortices have $\delta b_{\perp} \gg \delta b_{\parallel}$, as in the case of Alfvén vortices, but the majority of them are characterized by $\delta b_{\perp} \gtrsim \delta b_{\parallel}$. Thanks to multi-point measurements by the *Cluster* spacecraft, for about 100 structures we could determine the normal, the propagation velocity, and the spatial scale along this normal. Independently of the nature of the structures, the normal is always perpendicular to the local magnetic field, meaning that $k_{\perp} \gg k_{\parallel}$. The spatial scales of the studied structures are found to be between two and eight times the proton gyroradius. Most of them are simply convected by the wind, but 25% propagate in the plasma frame. Possible interpretations of the observed structures and the connection with plasma heating are discussed.

Key words: plasmas – solar wind – turbulence

1. INTRODUCTION

The interplanetary medium, a plasma that is almost collisionless, magnetized, and, despite being highly ionized, neutral, can be considered the best natural laboratory to study the dynamical behavior of turbulent plasmas. In situ spacecraft measurements generally reveal that the solar wind plasma is usually in a state of fully developed turbulence, where electromagnetic fields and plasma properties have a very large number of excited degrees of freedom (Bruno & Carbone 2005; Marsch 2006).

The large scales are essentially incompressible and the fluctuations of magnetic field and plasma velocity are often highly correlated, so that at times they can be thought of as nearly perfect Alfvén waves (Gosling et al. 2009; Matteini et al. 2014). The power spectra, in the inertial range of the turbulent cascade, manifest a behavior reminiscent of the Kolmogorov power law for fluid turbulence (Kolmogorov 1941; Matthaeus & Goldstein 1982; Tu & Marsch 1995). Then, the turbulent cascade extends to smaller spatial scales down to a wavelength range where kinetic effects govern the plasma dynamics. At these scales, around the proton characteristic lengths, different physical processes come into play, leading to a change in the spectral shape (Leamon et al. 1998, 2000; Bale et al. 2005; Smith et al. 2006; Alexandrova et al. 2007, 2008; Bourouaine et al. 2012). Although the origin of such variations is not yet well understood, a recent analysis by Bruno et al. (2014) has shown that the spectral slope above the frequency break is strongly related to the wind speed and to the power of the fluctuations within the inertial range; i.e., steeper spectra are found when speed and power are higher. Moreover, another important aspect, recovered at these scales, is an enhancement

of magnetic compressive fluctuations (Alexandrova et al. 2007, 2008; Hamilton et al. 2008; Salem et al. 2012; Kiyani et al. 2013), but the nature of the compressive component remains uncertain. At shorter scales (smaller than the proton characteristic scales and up to a fraction of the electron scales), the energy continues to be transferred and another spectrum is observed, whose interpretation is still controversial (Alexandrova et al. 2009, 2012; Sahraoui et al. 2010, 2013).

Although the physical mechanisms of solar wind turbulence have been matters of investigation for many decades, some of the primary problems concerning the nature of turbulent fluctuations along the turbulent cascade and the dissipation in a collisionless plasma still remain a puzzle. A fundamental question is whether space plasma turbulence can be considered a mixture of quasi-linear waves, as Alfvén waves at MHD scales (Matteini et al. 2014) and whistlers or kinetic Alfvén waves (KAW) at kinetic scales (Bale et al. 2005; He et al. 2011; Podesta & Gary 2011; Salem et al. 2012; Lacombe et al. 2014), or if the turbulence is strong with the formation of coherent structures responsible for intermittency and departure from self-similarity (Biskamp 1993; Frisch 1995), or even if the coexistence of both waves and structures is a more realistic vision (Newell et al. 2001; Roberts et al. 2013).

The intermittency phenomenon is the manifestation of non-uniform and inhomogeneous dissipation of the energy of a turbulent system (Frisch 1995). Different analyses have been focused on the characterization of intermittency in the solar wind (Burlaga 1991, 1993; Marsch & Tu 1994; Carbone et al. 1995, 1996; Horbury et al. 1997; Veltri & Mangeney 1999; Veltri 1999; Sorriso-Valvo et al. 2001, 2005; Bruno et al. 2003). Many of these studies are centered around the

departure of probability distribution functions (PDFs) from Gaussian statistics or the anomalous scaling of structure functions and relative deviations from self-similarity. These approaches are purely statistical and geometrical and do not provide any information on the physics of intermittency. An efficient way to study intermittency is given by the wavelet analysis method, through a decomposition of a signal into time–frequency space (Farge 1992). While the Fourier transform is inherently non-local (due to the nature of trigonometrical functions) and the information is completely delocalized among the spectral coefficients, wavelet transforms are able to catch localized events in time and frequency. It is important to note, however, that the choice of the mother function of the wavelet transform may favor the selection of different events: for example, the Haar wavelet (which is similar to a step function) will find mostly sharp discontinuities in the signal, while the Morlet mother function will favor wave-packet-like fluctuations.

In hydrodynamic turbulence, intermittency has been observed in the appearance of localized coherent structures in the vorticity field, spontaneously produced by non-linear dynamics (She et al. 1990; Frisch 1995). The characteristic length of these filaments of vorticity is of the order of the energy injection scale, while the cross-section is of the order of the dissipation scale. On the other hand, the appearance of coherent structures has also been observed in turbulent plasma systems. In the solar wind, in fact, the magnetic field has been found to be spatially characterized by abrupt changes, related to changes in plasma characteristics (e.g., particle heating). Their investigation has led to the discovering of a large variety of structures, with different properties. Recently, many efforts have been put forward to understand the nature of coherent structures by using in situ measurements (Bruno et al. 2001, 2007; Alexandrova et al. 2004, 2006; Sundkvist et al. 2005; Alexandrova & Saur 2008; Salem et al. 2009; Osman et al. 2011, 2012; Greco et al. 2012a; Perri et al. 2012; Zhdankin et al. 2012; Tessein et al. 2013; Greco & Perri 2014) and numerical data analysis (Greco et al. 2008, 2012b; Servidio et al. 2012, 2014a; Wan et al. 2012b, 2012a; Perrone et al. 2013b, 2014b; Wu et al. 2013; Haynes et al. 2015).

During the last years, the search for discontinuities in solar wind, by using the Haar wavelet (Veltri & Mangeney 1999) or the partial variance of increments (PVI) technique (Greco et al. 2008), resulted in finding one-dimensional current sheets in different regimes of the turbulent cascade (Veltri 1999; Bruno et al. 2001; Osman et al. 2011, 2012; Greco et al. 2012a; Perri et al. 2012; Greco & Perri 2014). An extensive study of these structures has shown that the current sheets are almost incompressible and pressure balanced, with the component of maximum variation that changes sign and is perpendicular to the mean magnetic field. Different examples of current sheets have been also recovered in other turbulent regions of the interplanetary medium, such as in the Earth’s magnetosheath (Retinò et al. 2007; Sundkvist et al. 2007; Chasapis et al. 2015), showing that thin current sheets are important sites of energy dissipation and particle heating.

Recently, Roberts et al. (2013), using the k -filtering technique (Pinçon & Lefeuvre 1991) and wave polarization analysis, have given some observational indications that the fast solar wind turbulence may be populated by KAW, small-scale current sheets, and by Alfvén vortices. The Alfvén vortex is one of the non-linear solutions of the ideal incompressible

MHD equations and it is characterized by magnetic and velocity fluctuations mostly perpendicular to the unperturbed magnetic field (Petviashvili & Pokhotelov 1992). Signatures of Alfvén vortices have been observed in the solar wind by Verkhoglyadova et al. (2003) at scales of the order of minutes. At scales close to the proton spectral break, Alfvén vortices have been observed for the first time in Earth’s and then in Saturn’s magnetosheaths (Alexandrova et al. 2006; Alexandrova & Saur 2008). Recently, large-amplitude Alfvén vortex-like structures at ion scales have been detected in a fast solar wind stream by Lion et al. (2016). A multi-satellite analysis of one well-defined Alfvén vortex in the slow wind can be found in Roberts et al. (2016).

Current sheets and Alfvén vortices are coherent structures with $\delta b_{\perp} \gg \delta b_{\parallel}$. However, very compressive structures, with $\delta b_{\parallel} \gg \delta b_{\perp}$, also exist, namely, magnetic solitons or magnetic holes. The term magnetic hole was introduced by Turner et al. (1977) to indicate a localized depression in the magnitude of the interplanetary magnetic field. More recently, Baumgärtel (1999) suggested an alternative description of magnetic hole, using the concept of magnetic soliton. Events of this class are usually believed to result from the mirror instability; that requires high plasma beta and a perpendicular temperature anisotropy (Winterhalter et al. 1994; Erdős & Balogh 1996; Génot et al. 2009). According to previous studies, these events are characterized by a localized change in the magnetic field accompanied by simultaneous changes in plasma density and kinetic pressure. The typical scales of these events cover a range from five seconds to several tens of seconds, which corresponds to a thickness from about 10 to several tens of proton inertial lengths (λ_p).

Rees et al. (2006) presented observational evidence for a class of structures that has the characteristics of solitons, using magnetic field measurements from the Ulysses magnetometer. These events appear as pulses in the magnetic field magnitude, associated with a rotation in the field direction itself. The duration of the impulsive events is of the order of 30 s, with the rotation lasting longer than the field enhancement. An approximate scale size of about $30 \lambda_p$ has been determined, in the direction parallel to the minimum variance direction, assuming that these structures are convected by the wind.

Multi-spacecraft observations of solitary structures have been performed by Stasiewicz et al. (2003), thanks to *Cluster* measurements in the magnetopause boundary layer, showing the existence of a slow-mode magnetosonic soliton with a short duration of 10 s observed by two spacecraft. This structure propagates close to a direction perpendicular to the mean magnetic field, with a speed of about 250 km s^{-1} with respect to the satellites (the velocity in the background medium cannot be completely determined because the structure is observed only by two spacecraft) and it has a perpendicular size of 1000–2000 km. More recently, Stevens & Kasper (2007) presented the first statistical study of magnetic-hole signatures in a steady solar wind, using *Wind* observations. These structures have been shown to be pressure-balanced events with similar properties from fluid to kinetic scales (from about 10^3 to 10 proton Larmor radii, ρ_p).

The aim of the present work is to study the nature of the turbulent fluctuations around the proton scales in the slow solar wind turbulent cascade, using high-time resolution magnetic field data from the *Cluster* spacecraft. For this purpose we use different tools of time series analysis. First, we apply a Morlet

wavelet transform in order to check if our signal is homogeneous or intermittent in time and frequencies. We also use wavelets to determine spectral properties of the signal and as a pass-band filter, to focus on the fluctuations around proton scales only. These fluctuations are more compressive than those within the inertial range. This property motivates us to focus our study on events with a finite compressive component. Second, in order to select intermittent events without any a priori idea of their shape (to be the most general possible), we use magnetic fluctuations around proton scales rather than the wavelet coefficients at these scales. As a result, we find that $\sim 40\%$ of the analyzed time interval (~ 600 events of several seconds during ~ 2 hr) is covered by coherent structures of different nature. Among them we observe linearly polarized compressive events like magnetic-hole-like, soliton-like, or shock structures; linearly polarized Alfvénic events (i.e., with dominant transverse fluctuations $\delta b_{\perp} > \delta b_{\parallel}$) like current sheets and elliptically polarized Alfvénic events, which look like magnetic vortices. Using the four *Cluster* satellites, we are able to characterize 109 (out of 600) structures in terms of the orientation of their normals and propagation in the plasma frame.

The paper is organized as follows: in Section 2 the selected data interval is described in terms of plasma parameters and turbulent behavior; in Section 3 the selection method for intermittent coherent events is presented and different coherent structures are given as examples; in Section 4 we show the results of statistical studies, using one- and multi-satellite approaches.

2. STUDIED TIME INTERVAL

The present study is based on in situ measurements from the *Cluster* mission in an interval of time (2002 February 19th) when the spacecraft was at apogee and in pure solar wind plasma. The same interval of three hours (00:00–03:00 UT) has been analyzed by Bale et al. (2005) and by Kellogg & Horbury (2005).

Different plasma experiments on board the *Cluster* spacecraft have been considered in order to characterize the observed solar wind stream. In particular, we consider high-resolution magnetic field data given by the fluxgate magnetometers (FGM) on *Cluster 1* (C1), with a sampling time of 22 Hz (Balogh et al. 2001). Proton data have been obtained from the Hot Ion Analyser (HIA) sensor of the Cluster Ion Spectrometry (CIS) experiment on C1 with a resolution of 4 s (Rème et al. 2001). For the electrons, two different experiments have been taken into account: the Plasma Electron and Current Experiment (PEACE) on C2 for electron temperature (no well-resolved PEACE data on C1 are available for the present interval) with a resolution of 4 s (Szita et al. 2001) and the Waves of High Frequency and Sounder for Probing of the Electron Density by Relaxation (WHISPER) on C1 with a resolution of 1.5 s (Décreau et al. 2001).

An overview of the considered time interval is summarized in Figure 1. Panels (a) and (b) show the magnitude of velocity and magnetic fields, respectively, where the bulk velocity in the spacecraft frame has been corrected for the $\sim 30 \text{ km s}^{-1}$ aberration produced by the orbital speed of the spacecraft and Earth around the Sun. The correction consists of subtracting $\sim 30 \text{ km s}^{-1}$ from the y_{GSE} component, because the y_{GSE} axis is anti-parallel to the direction of Earth’s motion. The present data set is representative of a slow solar wind, characterized by a

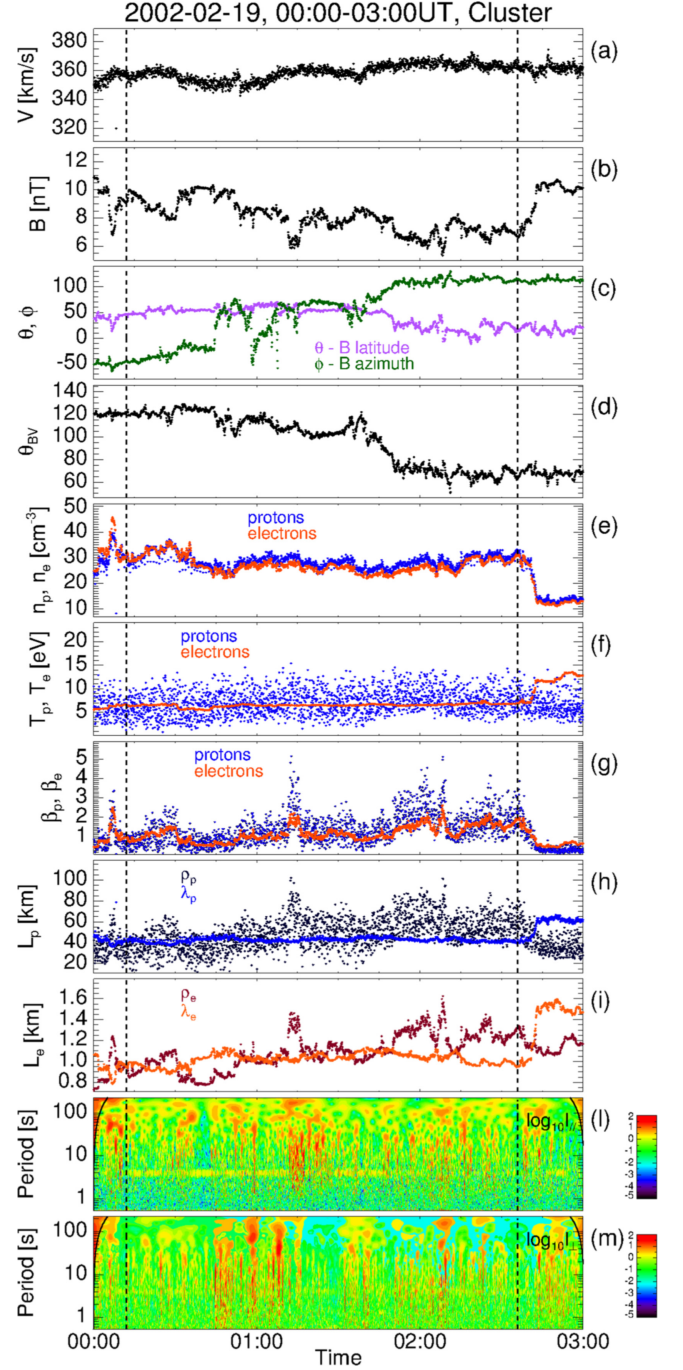


Figure 1. Overview of solar wind data for the time interval 00:00–03:00 UT on 2002 February 19th from *Cluster*. From top to bottom: magnitude of V (a) and B (b), latitude (θ , purple dots) and azimuth (ϕ , green dots) angles of B (c) and θ_{BV} (d); proton (blue dots) and electron (red dots) density (e), temperature (f) and plasma beta (g). Characteristic lengths for protons L_p (h) and electrons L_e (i); ρ_i (dark lines) and λ_i (light lines), with $i = p, e$. Logarithmic contour plots of LIM, $I(\tau, t)$ (see text), for parallel (l) and perpendicular (m) magnetic field fluctuations. Vertical dashed lines denote the time interval 00:12–02:36 UT used in the present analysis.

mean velocity of about 360 km s^{-1} and a mean magnetic field magnitude of about 9 nT. In panel (c), the temporal evolution of the latitude (θ , purple dots) and the azimuth (ϕ , green dots) angles of the magnetic field are displayed. A change in the behavior of these quantities is observed around 01:50 UT. θ is almost constant before this instant ($\sim 50^\circ$), then it starts to vary

between 0° and 50° . Conversely, the azimuthal component widely changes before this instant: ϕ starts at -50° , then abrupt magnetic field reversals are observed. After 01:50 UT, ϕ reaches 120° and remains almost steady. At the same time, a variation from 125° to 55° in the angle between magnetic and velocity fields, θ_{BV} , is observed (panel (d)).

Figure 1, panels (e) and (f), presents the density and the temperature, for protons (blue dots) and electrons (red dots), respectively. The two populations have about the same mean value for the total temperature. The large fluctuations in the proton temperature are essentially due to the digitization in energy, which for protons is $\sqrt{m_i/m_e}$ times worse than for electrons (I. Dandouras 2015, private communication). The mean plasma density is about $25\text{--}30\text{ cm}^{-3}$ before 02:45 UT and drops to about 10 cm^{-3} after this time. This density jump coincides with the jumps in temperature and in magnetic field magnitude, indicating a change of the solar wind stream. In this study we focus on the time interval 00:12–02:36 UT (between the two vertical dashed lines), which represents a more or less homogeneous solar wind.

Figure 1, panel (g), shows the plasma beta for protons (blue dots) and electrons (red dots), defined as the ratio between proton/electron kinetic pressure and magnetic pressure. Even if the values for β_p are scattered by the inaccuracy in the temperature determination, the mean value is about 1.5. In Bale et al. (2005), the average value for the proton beta is ~ 5 (about three times greater than in our case). This discrepancy comes from the fact that Bale et al. (2005) used CIS/CODIF data on C4 (S. Bale 2015, private communication) and we use here CIS/HIA data, more appropriate for the solar wind measurements. Although CODIF on C4 was operating on the low-sensitivity side during the solar wind mode, meaning that the solar wind beam has been correctly detected, CODIF is less accurate than HIA in the solar wind, due to the time-of-flight principle of operation. In fact, in solar wind, protons can saturate the CODIF instrument and, therefore, the moments of the ion distribution functions produced by CODIF can be incorrect (Rème et al. 1997).

Using the particle and field data, we could also determine the total pressure (not shown here). We found it to be almost constant during the studied time interval, with a mean value of $8 \times 10^{-2}\text{ nPa}$.

Figure 1, panel (h) shows the proton characteristic lengths, such as the Larmor radius and the inertial length. Panel (i) shows the same characteristic lengths for the electrons. The Larmor radii, $\rho_{p,e}$ (dark dots), are defined as the ratio between the perpendicular thermal speeds ($v_{th}^{(p,e)} = \sqrt{2kT_{\perp}^{(p,e)}/m_{p,e}}$), and the particle cyclotron frequencies, $\omega_c^{(p,e)}$. The inertial lengths, $\lambda_{p,e}$ (light dots) are defined as the ratio between the light speed, c , and the particle plasma frequencies, $\omega_p^{(p,e)}$.

Figure 1, panels (l) and (m), shows the evolution of the energy of magnetic fluctuations (parallel and perpendicular to B_0 , respectively) in time and at different scales, normalized at each time point by a mean spectrum over the whole time interval.

The decomposition in time, t , and scales, τ , is done using the wavelet transform:

$$\mathcal{W}_i(\tau, t) = \sum_{m=0}^{N-1} B_i(t_m) \psi^*[(t_m - t)/\tau], \quad (1)$$

where $B_i(t_j)$ is the i th component of the magnetic field and ψ^* is the conjugate of a wavelet function. The mother function used in the present analysis is the Morlet wavelet

$$\psi(u) = 2^{1/2} \pi^{-1/4} \cos(\omega_0 u) \exp(-u^2/2), \quad (2)$$

which consists of a plane wave modulated by a Gaussian, where ω_0 is the non-dimensional frequency and is taken to be 6 to satisfy the admissibility condition (Farge 1992).

The compressive fluctuations (panel (l)) are approximated by the variations of magnetic field magnitude, so the corresponding energy is

$$\mathcal{W}_{\parallel}^2(\tau, t) = \mathcal{W}_{|B|}^2(\tau, t). \quad (3)$$

Independently of the definition of a mean magnetic field, B_0 , this approximation is valid when the level of fluctuations is much lower than B_0 ($\delta B/B_0 \ll 1$). In this case, we can write

$$|B|^2 = (\mathbf{B} \cdot \mathbf{B}) = (\mathbf{B}_0 + \delta \mathbf{B})^2 \simeq B_0^2 + 2\delta \mathbf{B} \cdot \mathbf{B}_0, \quad (4)$$

then the variations of the field amplitude is

$$\delta|B|^2 = |B|^2 - B_0^2 = 2\delta \mathbf{B} \cdot \mathbf{B}_0 = 2\delta B_{\parallel} B_0 \simeq \delta B_{\parallel}^2. \quad (5)$$

Knowing the total energy of magnetic fluctuations as a function of time and scale

$$\mathcal{W}_B^2(\tau, t) = \sum_i \mathcal{W}_i^2(\tau, t), \quad i = x, y, z, \quad (6)$$

we define the energy of Alfvénic (or transverse to the mean field) fluctuations, independently of B_0 , as

$$\mathcal{W}_{\perp}^2(\tau, t) = \mathcal{W}_B^2(\tau, t) - \mathcal{W}_{\parallel}^2(\tau, t). \quad (7)$$

The normalization used in Figure 1, panels (l) and (m), is the following:

$$I_{\parallel,\perp}(\tau, t) = \frac{|\mathcal{W}_{\parallel,\perp}(\tau, t)|^2}{\langle |\mathcal{W}_{\parallel,\perp}(\tau, t)|^2 \rangle_t}, \quad (8)$$

where the angled brackets indicate the time average. In the literature it is called the Local Intermittency Measure (LIM; Farge 1992). It is worth pointing out that the horizontal light band, in panel (l), around 4 s is due to the spin satellite frequency. The curved black lines, on each side of the plots, represent the cone of influence, where the Morlet coefficients are affected by edge effects (Torrence & Compo 1998).

LIM representation helps to see small (and less energetic) scales in more detail. In Figure 1, panels (l) and (m), one observes a non-homogeneous distribution of magnetic energy in time with appearance of localized energetic events covering a range of scales: an inherent property of intermittent coherent structures (Frisch 1995). We will study these structures in the next section of the paper. Before that, we consider statistical properties of the studied turbulent flow.

Figure 2(a) shows the total power spectral density (PSD) of magnetic fluctuations $S(f) = \sum_{i=x,y,z} S_i(f)$ (solid line). S_i is the PSD of the B_i component, defined as

$$S_i(\tau) = \frac{2\delta t}{N} \sum_{j=0}^{N-1} |\mathcal{W}_i(\tau, t_j)|^2, \quad i = x, y, z, \quad (9)$$

where δt represents the time spacing. The frequency dependence is easily obtained using the $f = 1/\tau$ relationship. In the MHD range, $S(f)$ manifests the typical behavior of the

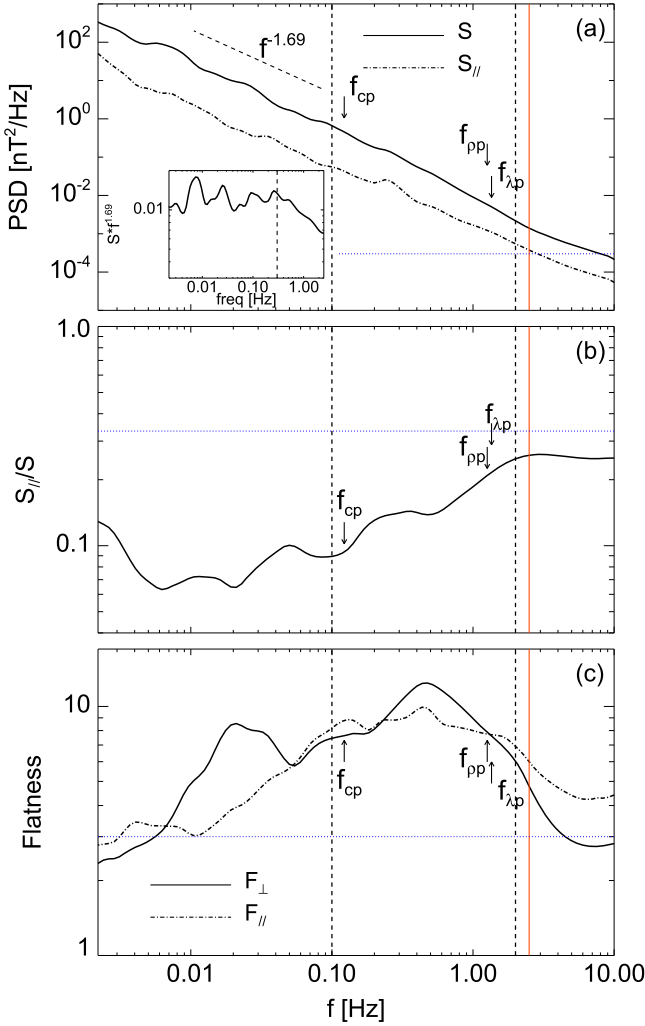


Figure 2. Panel (a): PSD of total (S , solid line) and compressive ($S_{||}$, dash-dot line) magnetic fluctuations. The horizontal blue dotted line indicates the $S/N = 3$. The insert in panel (a) shows the compensated spectrum $S * f^{1.69}$. Panel (b): level of compressibility of magnetic fluctuations ($S_{||}/S$) as a function of frequency. The horizontal blue dotted line refers to the isotropic case. Panel (c): flatness for Alfvénic (F_{\perp} , solid line) and compressive ($F_{||}$, dash-dot line) magnetic fluctuations. The value of the flatness for a standard normal distribution (horizontal blue dotted line) is given as reference. The vertical red solid line indicates the maximum resolved frequency for the spectra ($f_{\max} = 2.5$ Hz).

Kolmogorov power law, $f^{-1.69}$. Then, the spectrum changes its slope at ~ 0.3 Hz, that is, between the proton cyclotron frequency f_{cp} and Doppler shifted proton Larmor radius $f_{\rho_p} = v_{sw}/2\pi\rho_p$ and proton inertia length $f_{\lambda_p} = v_{sw}/2\pi\lambda_p$ (estimated under the assumption of wave vector parallel to the plasma flow, see the arrows in the plot). This is more visible in the insert of panel (a), where a compensated spectrum $S(f) \cdot f^{1.69}$ is displayed.

In order to study kinetic scales, we should, first, determine the frequency range where the measurements are not affected by the instrumental noise. The digitization of the *Cluster*/FGM instrument in the solar wind mode is 10^{-2} nT, and therefore in the spectrum it appears at 10^{-4} nT² Hz⁻¹ for a one-component spectrum. So, for the total PSD, $S_{\text{noise}} = 3 \times 10^{-4}$ nT² Hz⁻¹. We fix the maximum resolved frequency for the spectra at $f_{\max} \simeq 2.5$ Hz (vertical red solid line), which corresponds to a

signal-to-noise ratio (S/N) for a one-component spectrum equal to 3 (and for the total spectrum, equal to 9); see the horizontal blue dotted line. Therefore, in the kinetic range, we can study the frequency range $f = [0.3, 2.5]$ Hz, which is nearly one decade. Within this range, the total PSD becomes steeper, with a spectral slope of $\simeq -2$. It is in agreement with the recent results of Bruno et al. (2014) for slow solar wind spectra.

The PSD of the compressive fluctuations

$$S_{||}(\tau) = \frac{2\delta t}{N} \sum_{j=0}^{N-1} |\mathcal{W}_{||}(\tau, t_j)|^2 \quad (10)$$

is shown by dash-dot line in Figure 2(a). It follows $S(f)$ in the MHD range of scales. A small bump of compressive energy around 0.25 Hz corresponds to the satellite spin, visible in the Morlet scalogram (panel (l) of Figure 1) as a horizontal band around $\tau = 4$ s.

Figure 2(b) shows the level of compressibility of magnetic turbulent fluctuations as a function of frequency, defined as $S_{||}(f)/S(f)$. The horizontal blue dotted line indicates the isotropic case $S_{||} = S/3$. The level of compressive fluctuations starts to increase at the end of the MHD range and continues around proton characteristic scales as was already observed by Alexandrova et al. (2008), Salem et al. (2012), and Kiyani et al. (2013). In our study, unfortunately, we have no information on sub-ion scales compressibility, because the maximal frequency is very close to (but higher than) the highest ion characteristic frequency (f_{λ_p}). However, with our data we can study in detail a frequency range around all ion scales, i.e., $[0.1, 2]$ Hz (see vertical black dashed lines), where the increase of compressibility is observed.

Figure 2(c) shows the fourth-order moment of compressive (dash-dot line) and Alfvénic (solid line) magnetic fluctuations, defined as

$$F_{||,\perp}(\tau) = \frac{\langle \tilde{\mathcal{W}}_{||,\perp}(\tau, t)^4 \rangle}{\langle \tilde{\mathcal{W}}_{||,\perp}(\tau, t)^2 \rangle^2}, \quad (11)$$

where $\tilde{\mathcal{W}}$ is the real part of the wavelet coefficients. The value for the flatness of a standard normal distribution is 3, indicated on the plot by a horizontal blue dotted line. The study of solar wind turbulence suggests that the intermittency increases when considering smaller and smaller scales or, equivalently, higher and higher frequencies, starting from MHD scales (Bruno et al. 2003). In our case, we are not able to catch non-Gaussian contributions at large scales because of the limited length of the data set (~ 2 hr). However, we observe that, at the end of the MHD range, both curves of flatness depart from the value of flatness of the normal distribution. Note that, here, we calculate flatness of Alfvénic fluctuations using the definition (7). If we project $\delta\mathbf{B}$ in the mean field frame (with the mean field \mathbf{B}_0 defined as a mean over the total interval of study), we can calculate the flatness of two perpendicular components. We find that the flatness F_{\perp} , shown in Figure 2(c), corresponds to the median of the two perpendicular components.

Between the proton characteristic scales, the flatness of compressive fluctuations, $F_{||}(f)$, becomes more or less constant while the flatness of transverse fluctuations $F_{\perp}(f)$ reaches its maximum at ~ 0.4 – 0.5 Hz and then starts to decrease. Another local maximum of F_{\perp} is observed around 0.02 Hz, which is about $0.2f_{cp}$, i.e., the frequency where Alfvén Ion Cyclotron

(AIC) waves can be unstable. (However, AIC waves are out of the scope of the present paper.) The observed fluctuating behavior of flatness reflects the non-homogeneous distribution of turbulent fluctuations, as observed in the Morlet wavelet scalograms of Figure 1.

In the following part of the paper, we will focus on a range of scales just around ion scales, $f \in [0.1, 2]$ Hz (denoted in Figure 2 by vertical dashed lines), which corresponds to a timescale range $\tau \in [0.5, 10]$ s.

3. IDENTIFICATION OF INTERMITTENT EVENTS

3.1. Method

The magnetic field fluctuations in a particular scale range can be defined using a bandpass filter based on the wavelet transform (Torrence & Combo 1998; He et al. 2012; Roberts et al. 2013)

$$\delta b_i(t) = \frac{\delta j \delta t^{1/2}}{C_\delta \psi_0(0)} \sum_{j=j_1}^{j_2} \frac{\tilde{\mathcal{W}}_i(\tau_j, t)}{\tau_j^{1/2}}, \quad (12)$$

where j is the scale index and δj is the constant step in scales; the factor $\psi_0(0) = \pi^{1/4}$ and the value of the constant C_δ , which is derived from the reconstruction of a δ function using the Morlet wavelet, is 0.776 (Torrence & Combo 1998). Here we use $\tau(j_1) = 0.5$ s and $\tau(j_2) = 10$ s to study scales (and frequencies) around ion scales.

As we have seen in Figure 2(b), at scales around ion scales, the compressibility increases. Let us consider these compressive fluctuations, which we denote δb_{\parallel} . Figure 3(a) displays the time evolution of δb_{\parallel} , defined by Equation (12) with \mathcal{W}_{\parallel} , and normalized to the mean magnetic field over the whole time interval under study, $\delta b_{\parallel}/B_0$. The PDF of δb_{\parallel} , normalized to its own standard deviation $\sigma(\delta b_{\parallel})$, is shown in panel (b) (black solid line) and it is compared to the corresponding Gaussian fit (black dashed line): the present non-Gaussian tails are characteristic of some intermittency or inhomogeneity of the turbulence (Frisch 1995). The vertical red solid lines indicate the position of three standard deviations of the Gaussian fit, which include 99.7% of the Gaussian contribution. All the events that exceed this limit contribute to the non-Gaussian part of the PDF. This value will be used as a threshold to select non-Gaussian compressive intermittent events.

Figure 3(c) shows a zoom of $\delta b_{\parallel}^2(t)$, during one minute (black solid line). An envelope of the energy of magnetic fluctuations is indicated by the blue solid line and defined as the smooth curve outlining the extremes of the oscillating signal. The corresponding threshold in the energy ($\delta b_{\parallel}^2 = 3.9 \times 10^{-2} \text{ nT}^2$) is shown by the horizontal red solid line. The maxima of the energy of the intermittent events over this threshold are marked by red stars. We define the width of an event $\Delta\tau'$ as the time range between the two minima of the envelope, containing a maximum of the energy over the threshold. Then the characteristic temporal scale of an event, $\Delta\tau$, can be defined as the width at half height (intersection of the black dashed lines in panel (c)).

During the one-minute time interval shown in Figure 3(c), we observe three intermittent events. For the whole time interval under study we get about 600 events. The characteristic timescale of these events varies in the range $\Delta\tau \in [0.25, 7]$ s and the width $\Delta\tau' \in [0.75, 7.5]$ s.

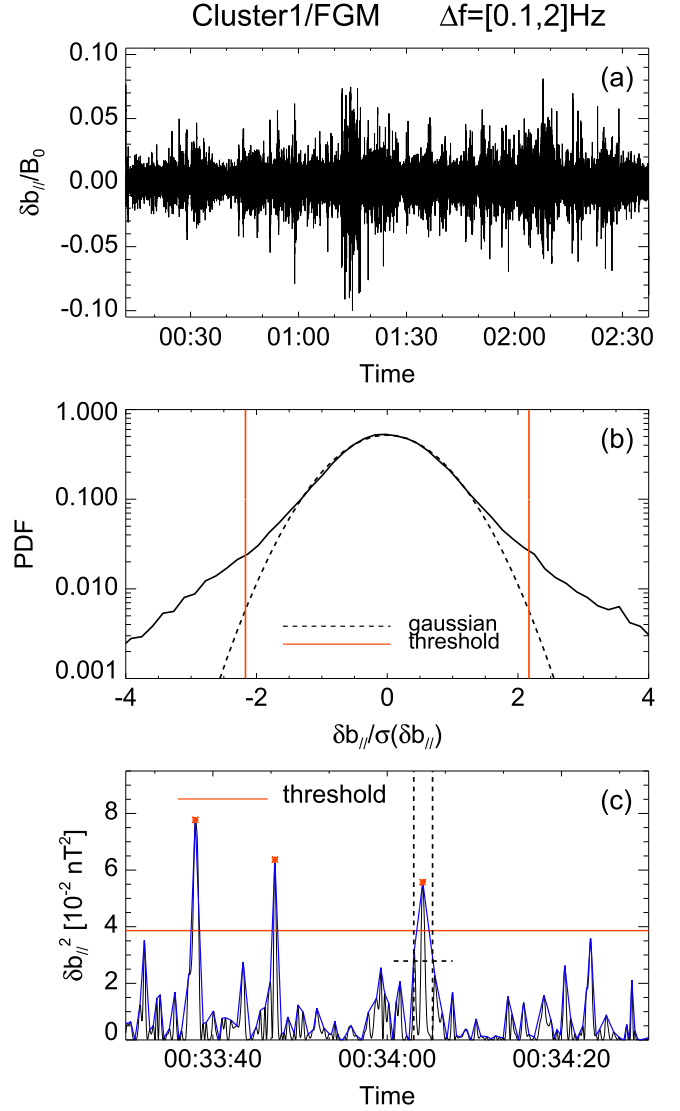


Figure 3. Panel (a): time evolution of compressive fluctuations, δb_{\parallel} , in the frequency range $[0.1, 2]$ Hz, normalized to the mean magnetic field B_0 . Panel (b): PDF of δb_{\parallel} , normalized to $\sigma(\delta b_{\parallel})$, (black solid line) and the corresponding Gaussian fit (black dashed line). The vertical red solid lines indicate the position of three standard deviations of the Gaussian fit, used to determine the threshold in panel (c). Panel (c): zoom of the compressive energy, δb_{\parallel}^2 . The blue solid line is an envelope of the magnetic energy, the red stars indicate the maximum of the energy of the intermittent events (i.e., events with the energy over the threshold, shown by the red solid line) and the dashed lines show how to define the characteristic temporal scale of an event (width at half height).

3.2. Examples

By performing a minimum variance analysis around the 600 events, we could identify by eye six different families. Figures 4–11 show some examples of these families, in different time ranges (from about 4 to 7 $\Delta\tau'$), depending on the presence of other events in the close vicinity of the considered one. These intermittent events are well localized in time and have regular magnetic field profiles. We can identify them as coherent structures. For a subset of 109 structures (which also contains the examples in Figures 4–8 and 10–11), we were able to study the orientation of their normals and the propagation in the plasma frame.

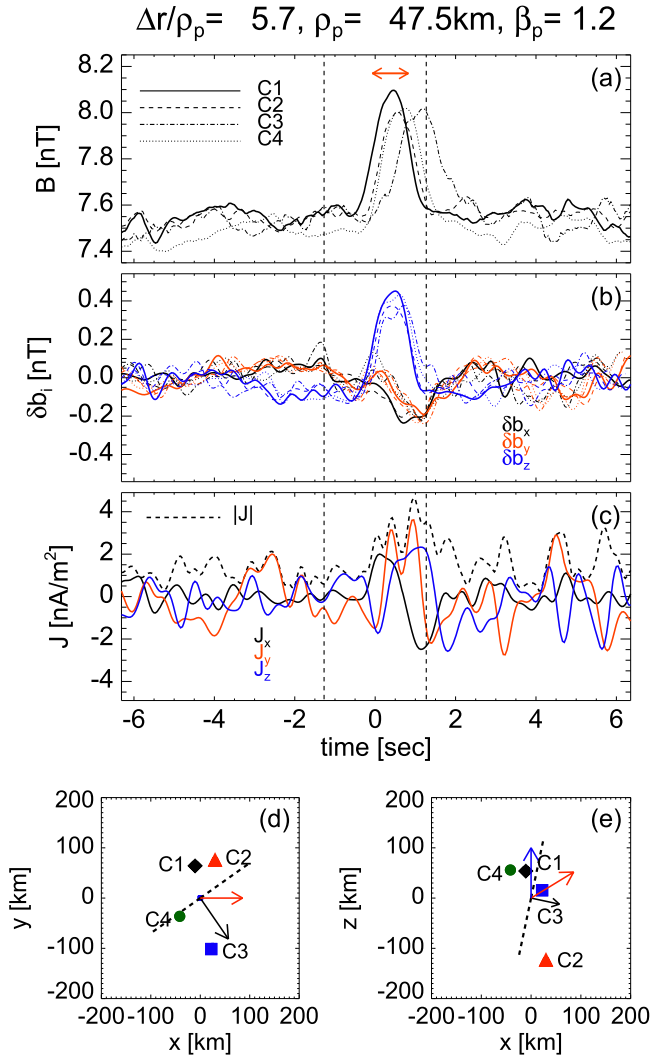


Figure 4. Example of linearly polarized compressive soliton-like structure, centered at 02:10:42.5 UT. Panel (a): modulus of the large-scale magnetic field observed by the four *Cluster* satellites (different style lines). The red double arrow indicates $\Delta\tau$, corresponding to Δr defined in Section 4.2.1. Panel (b): components of magnetic fluctuations defined by Equation (12), in the BV -frame. The time of each satellite is shifted taking into account the time delays with respect to C1. Panel (c): modulus (black dashed line) and components (in BV -frame) of the current density. The vertical black dashed lines indicate $\Delta\tau'$, corresponding to the total extension of the structure ($\Delta r' = 16.3\rho_p$). Panels (d) and (e): configuration of *Cluster* satellites in BV -frame: black diamonds for C1, red triangles for C2, blue squares for C3, and green circles for C4. The arrows indicate the direction of the normal (black), local flow (red), and local magnetic field (blue), while the black dashed lines represent the plane of the structure.

3.2.1. Strongly Compressive Structures

Soliton and magnetic holes. The first three examples of coherent structures are shown in Figures 4–6. Panel (a) displays the modulus of the raw magnetic field measurements, as observed by the four satellites, where the FGM noise at $f > 2.5$ Hz is taken off. In the following part of the paper, we refer to it as the large-scale magnetic field. The different line styles correspond to different satellites of *Cluster*, as indicated in the legend. The red double arrow indicates $\Delta\tau$, i.e., the characteristic temporal scale of the structures (width at half height).

The structures appear as an impulse (increase or decrease) in the ambient magnetic field, looking like a magnetic hump or

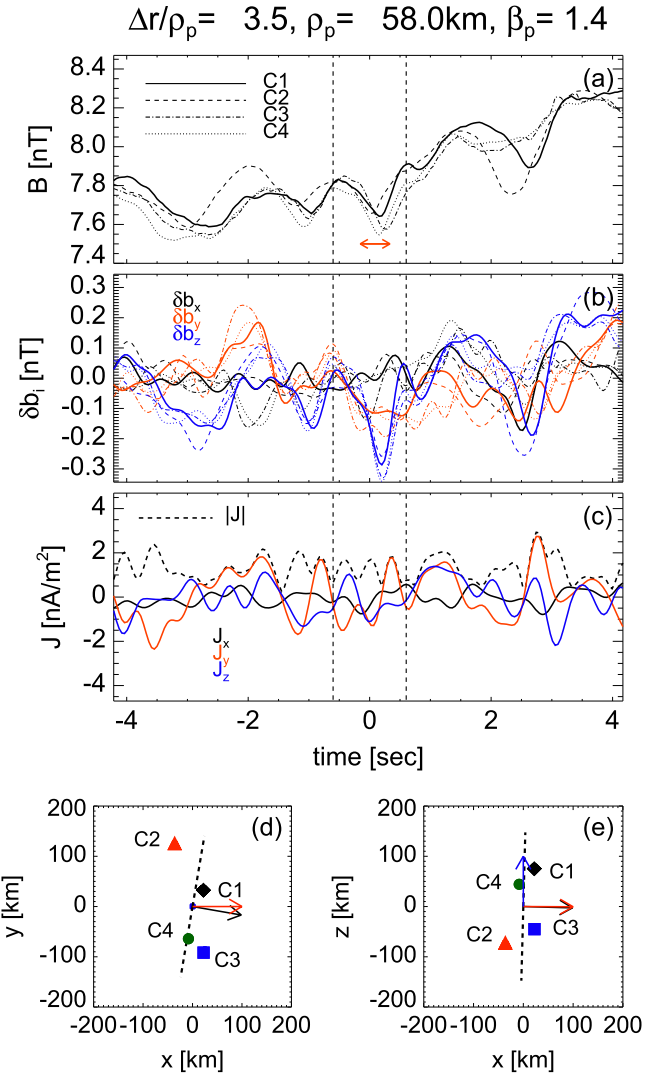


Figure 5. Example of linearly polarized and compressive chain of magnetic-hole-like structures, centered at 01:47:15.7 UT and with $\Delta r' = 8.6\rho_p$. The panels are the same as in Figure 4.

soliton and magnetic holes, respectively. By looking outside the width of these structures ($\Delta\tau'$, indicated by the two vertical dashed lines), we observe that, while the soliton is a quite solitary hump (Figure 4), the magnetic hole in Figure 5 seems to be only one structure in a chain of structures. A careful inspection of the 600 structures shows that usually magnetic holes appear in the plasma as a chain of compressive structures, while solitons are observed as isolated structures. However, a few examples of solitary depression are also observed and an example is given in Figure 6.

In panels (b), magnetic fluctuations δb_i (with $i = x, y, z$), defined by Equation (12), are shown in the reference frame, which takes into account the directions of the local mean magnetic field \mathbf{b}_0 and flow velocity \mathbf{v}_0 defined within each structure timescale $\Delta\tau'$ (time between two vertical dashed lines): z is aligned with the local \mathbf{b}_0 , $\mathbf{e}_z = \mathbf{e}_b$ (blue lines), x is aligned with \mathbf{v}_0 in the plane perpendicular to \mathbf{b}_0 , $\mathbf{e}_x = (\mathbf{e}_b \times \mathbf{e}_v) \times \mathbf{e}_b$ (black lines) and y closes the right-hand reference frame, $\mathbf{e}_y = \mathbf{e}_b \times \mathbf{e}_x$ (red lines). Below, we refer to this frame as BV -frame. Here, the time of each satellite is shifted, taking into account the time delays with respect to C1.

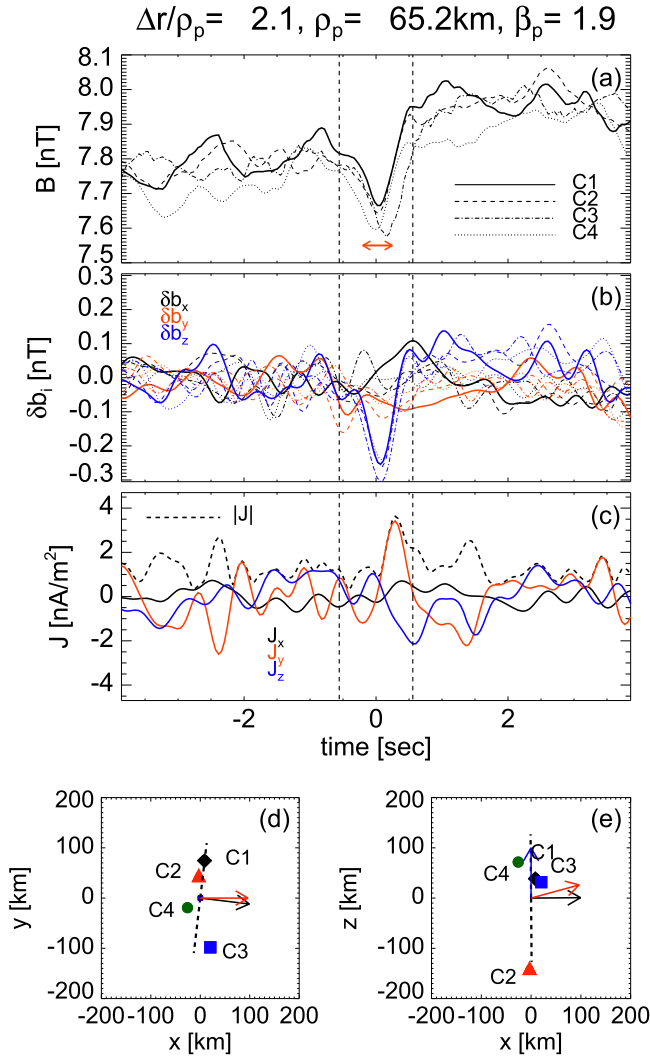


Figure 6. Example of linearly polarized and compressive solitary magnetic-hole-like structure, centered at 02:14:08.2 UT and with $\Delta r' = 5.3\rho_p$. The panels are the same as in Figure 4.

All the structures shown in Figures 4–6 are strongly compressive: the maximal variation is δb_z , as observed in panels (b). In order to quantify the compressibility of the structures, we evaluate a local compressibility parameter, ξ_{\parallel} , defined as the ratio between parallel and perpendicular contributions. In particular,

$$\xi_{\parallel} = \sqrt{\frac{\max(\delta b_z^2)}{\max(\delta b_x^2 + \delta b_y^2)}}, \quad (13)$$

where the maximum of the magnetic components is evaluated within $\Delta\tau'$. For the selected compressive structures, we found $\xi_{\parallel} = 1.6$ for the soliton, 2.1 for the chain of magnetic holes and 1.8 for the solitary magnetic hole.

Minimum variance analysis applied to these structures confirms the previous results: the direction of the maximal variation \mathbf{e}_{\max} is close to the direction of \mathbf{b}_0 . In particular, the angle between these two directions, θ_{\max} , is $\simeq 15^\circ$ for the soliton, $\simeq 16^\circ$ for the chain, and $\simeq 12^\circ$ for the solitary magnetic hole. Furthermore, the minimum variance \mathbf{e}_{\min} is strictly perpendicular to \mathbf{b}_0 for both examples of magnetic holes and

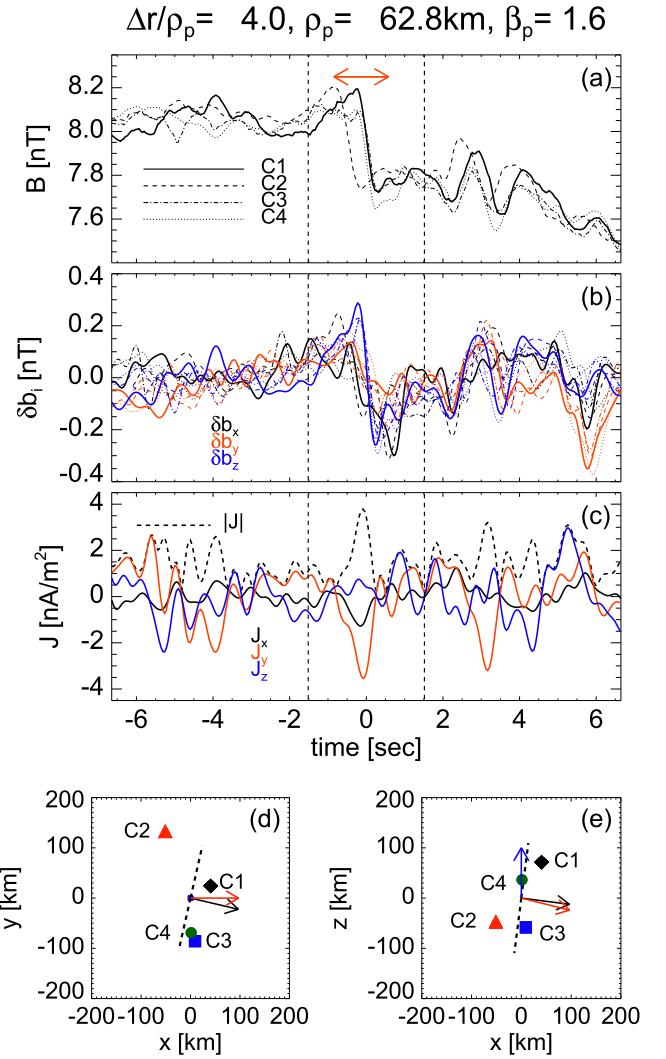


Figure 7. Example of linearly polarized compressive shock-like structure, centered at 01:17:44.9 UT and with $\Delta r' = 8.4\rho_p$. The panels are the same as in Figure 4.

nearly perpendicular for the soliton-like structure ($\theta_{\min} \simeq 83^\circ$ and $\theta_{\text{int}} \simeq 77^\circ$).

Panel (c) in Figures 4–6 displays the evolution of the current density \mathbf{J} , calculated using the curlometer technique (Dunlop et al. 1988, 2002) based on four-point measurements of *Cluster*. The three components of \mathbf{J} are given in the *BV*-frame; the modulus, $|\mathbf{J}|$, is shown by the dashed line. The curlometer technique works well in our case, as far as the four satellites are inside the same event during most of the time of the width of the structure $\Delta\tau'$. The factor $Q = \text{div } \mathbf{B} / \text{curl } \mathbf{B}$ is usually used as a quality factor of the calculation of gradients. In our case it is very good ($Q \ll 1$ within $\Delta\tau'$). Note, however, that $\text{div } \mathbf{B}$ and $\text{curl } \mathbf{B}$ include different gradients, so it is difficult to assess whether or not Q can indeed play the role of a quality factor (G. Chanteur 2015, private communication). The current density \mathbf{J} is almost perpendicular to \mathbf{b}_0 in the case of the holes, while it is more oblique in the case of the soliton.

Finally, panels (d) and (e) show the configuration of the four *Cluster* satellites in the *BV*-frame, by using different symbols and colors, as indicated in the caption of Figure 4. The arrows display the directions of the normal of the structures, \mathbf{n} (black), determined by using the timing method (see Section 4.2.1), of

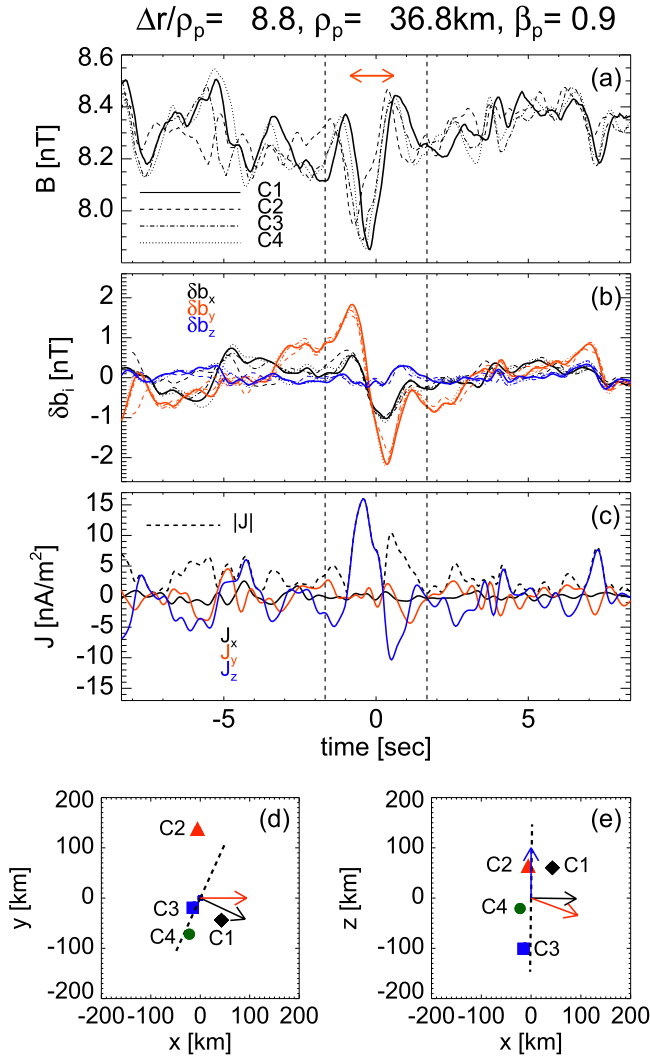


Figure 8. Example of a current sheet, centered at 01:07:37.8 UT and with $\Delta r' = 30.1\rho_p$. The panels are the same as in Figure 4.

ν_0 (red) and of \mathbf{b}_0 (blue). Moreover, the black dashed lines indicate the plane of the structures. For the magnetic holes, we have \mathbf{n} strictly perpendicular to \mathbf{b}_0 , while for the soliton we have $\Theta_{nB} = 83^\circ \pm 15^\circ$. Moreover, if \mathbf{n} of the chain of magnetic holes and for the solitary magnetic hole is nearly aligned with the solar wind flow speed in the (x, y) -plane ($\Theta_{nV_\perp} = 10^\circ \pm 10^\circ$ and $7^\circ \pm 8^\circ$, respectively), \mathbf{n} of the magnetic soliton is oblique to it ($\Theta_{nV_\perp} = 55^\circ \pm 20^\circ$). The propagation velocity of the structures along \mathbf{n} in the plasma rest frame (see Section 4.2.2) is $\mathcal{V}_0 = (55 \pm 92) \text{ km s}^{-1}$ and $-(35 \pm 71) \text{ km s}^{-1}$ for the chain of magnetic holes and for the solitary magnetic hole, respectively, and $\mathcal{V}_0 = (151 \pm 97) \text{ km s}^{-1}$ for the soliton ($V_A = 32 \text{ km s}^{-1}$ and $V_F = 54 \text{ km s}^{-1}$). While the magnetic holes are simply convected in the limit of the errors by the wind, the soliton-like structure has a finite velocity in the plasma rest frame.

The normal to the structures was determined assuming that the structure is locally planar, i.e., that holes and soliton may have an infinite front in the plane perpendicular to \mathbf{n} . The results show that \mathbf{n} is perpendicular to \mathbf{b}_0 and the latter is in the plane of the front (see panel (e)). However, this front seems to be perturbed or finite, especially in case of the magnetic holes. Indeed, for example from Figure 5, one can see that the

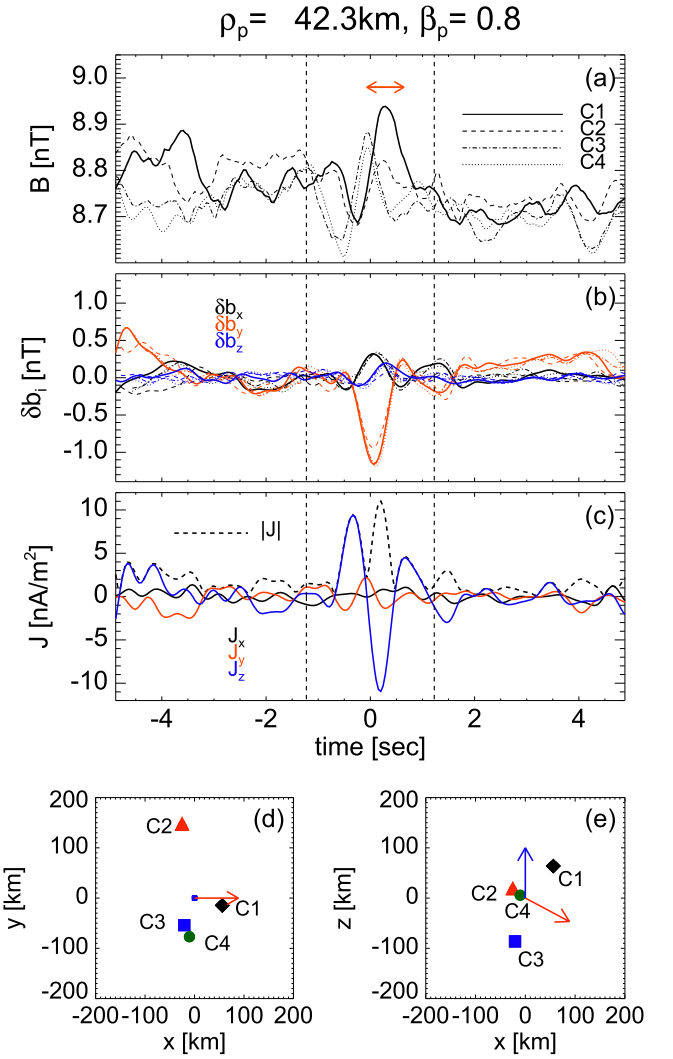


Figure 9. Example of solitary Alfvén vortex, centered at 00:56:16.1 UT. For this event, it was not possible to apply the four-satellite timing method; therefore the exact values of Δr and $\Delta r'$ are not known. The panels are the same as in Figure 4, except for panels (d) and (e), where no indication about the direction of the normal and the plane of the structure is given.

different satellites observe different amplitudes: satellite C2 (red triangles) sees the event first, then C4 (green circles) and C1 (black diamonds) see the signal, nearly at the same time, but with different amplitudes, and C3 (blue squares) is the last to observe the signal, seeing almost the same amplitude observed by C4. Such variation in amplitude cannot be explained by an infinite plane; in that case, all satellites would see the same amplitude in each point of the plane. Therefore, the structure is not perfectly planar. If a magnetic hole is a cylinder (or a cigar) with an axis along \mathbf{b}_0 , variations of the amplitude from one satellite to another are related to the fact that different satellites cross the structure at different distances from its axis. Along the axis the signal is expected to be the same, as it is indeed observed on C3 and C4, separated along \mathbf{b}_0 by ~ 100 km and very close in the perpendicular plane.

In the case of the magnetic soliton, the amplitudes of the magnetic fluctuations (see Figure 4(b)) are nearly the same on the four satellites, indicating that the topology of the structure is not far from the planar front. This front is going through C2

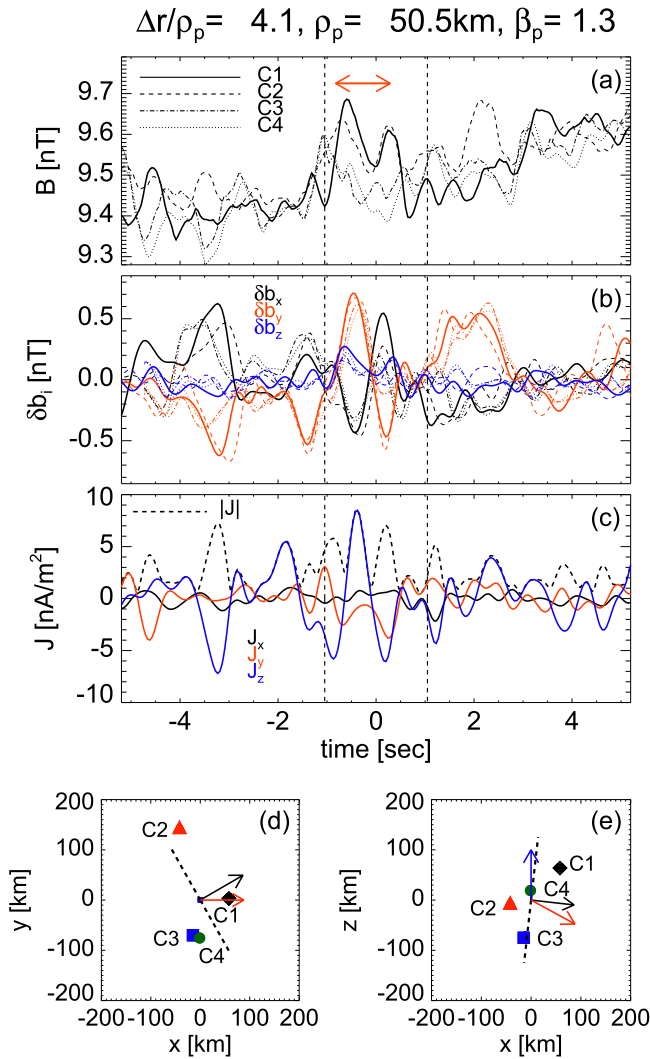


Figure 10. Example of Alfvén vortex-like structure, centered at 00:49:58.5 UT and with $\Delta r' = 7.7\rho_p$. The panels are the same as in Figure 4.

and C4 in the (x, y) -plane (see panel (d)). Note that these satellites observe the same signal at the same time.

To conclude on the geometry of the discussed compressive structures, a comparison of the signals on the four satellites with different geometrical models of holes and solitons should be done (a subject of our future work).

In terms of plasma parameters: the soliton is observed for $\beta_p \simeq 1.2$, while the magnetic holes appear at a higher value of local plasma beta (1.4 for the chain and 1.9 for the solitary magnetic hole). The time localization is different as well: the magnetic soliton is nearly two times larger with respect to the magnetic holes. In terms of normalized spatial scales (see Section 4.2.1), the magnetic hole in the chain is $\sim 3.5\rho_p$, while the solitary magnetic hole is $\sim 2\rho_p$; and the soliton-like structure is $\sim 6\rho_p$. These structures differ also by the values of the local proton temperature anisotropy $A = T_\perp/T_\parallel$: within the magnetic holes $A \simeq 2$, while within the soliton the protons are nearly isotropic ($A \simeq 1.1$).

In the subset of 109 structures, we have observed 10 magnetic holes, considering both magnetic holes in the chains and solitary magnetic holes, and 6 solitons. The magnetic holes present the characteristics of mirror mode structures (Soucek et al. 2008; Génot et al. 2009): high values of temperature

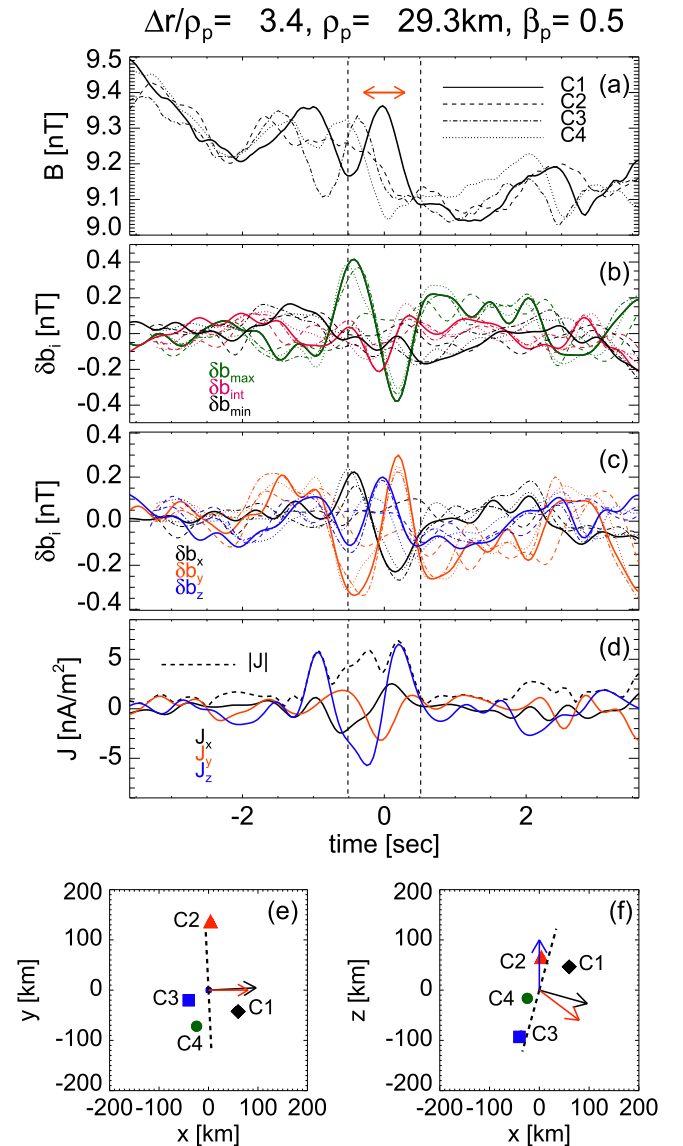


Figure 11. Example of compressive vortex-like structure, centered at 00:31:10.4 UT. Panel (a): modulus of the large-scale magnetic field observed by the four *Cluster* satellites (different style lines). The red double arrow indicates Δr , corresponding to Δr . Panel (b): components of magnetic fluctuations defined by Equation (12), in minimum variance frame. The maximum direction is in green, the intermediate in red, and the minimum in black. The time of each satellite is shifted taking into account the time delays with respect to C1. Panel (c): same representation as in panel (b), but in BV -frame. Panel (d): modulus (black dashed line) and components (in BV -frame) of the current density. The vertical black dashed lines indicate $\Delta r'$ of the structure, corresponding to $\Delta r' = 6.1\rho_p$. Panels (e) and (f): configuration of *Cluster* in BV -frame: black diamonds for C1, red triangles for C2, blue squares for C3, and green circles for C4. The arrows indicate the direction of the normal (black), local flow (red), and local magnetic field (blue), while the black dashed lines represent the plane of the structure.

anisotropy and plasma beta, and they are simply convected by the flow in the limits of the errors. Moreover, if we evaluate the mirror parameter, C_M ,⁵ as defined in Equation (4) of Génot et al. (2009), we obtain the result that almost all the magnetic holes are observed under mirror unstable plasma conditions ($C_M > 1$). It is worth pointing out that C_M is obtained for

⁵ The values of the perpendicular plasma beta and of the temperature have to be considered in a region of the ambient plasma near the structures and in our case we evaluate them at the borders of the structures.

bi-Maxwellian distribution functions, in the low-frequency, long-wavelength limit of the Vlasov-Maxwell equations and in the case of cold electrons. Moreover, the particle detector used for the analysis (CIS/HIA) bins the ions according to their energy per charge ratio. Therefore, protons and alpha particles are generally mixed and moments are averaged. For the structures shown in Figures 5 and 6, we have $C_M = 1.7$ and 1.9, respectively. However, some examples of magnetic holes under stable mirror conditions ($C_M < 1$) are also found. These observations could have different explanations. First of all, as we do the evaluation of C_M automatically for 600 structures, it is possible that the borders of some structures, especially for the chains of magnetic holes, are not properly determined. Therefore, the evaluation of C_M , which should be done outside of the structures where we suppose to have an ambient plasma, could be mistaken. On the other hand, it is possible that the holes, found in stable conditions, are generated elsewhere, where the plasma was unstable, and convected away by the wind. It could be also possible that these magnetic holes are indeed the result of the mirror instability, but we observe them when the surrounding plasma becomes stable after the instability.

For the magnetic solitons, we have a completely different situation: the plasma beta is moderate ($\langle\beta_p\rangle \sim 1.2$) and the ion temperature is almost isotropic ($\langle T_\perp/T_\parallel \rangle \sim 1.2$), which corresponds to $C_M < 1$. In particular, for the example in Figure 4, we have $C_M = 0.1$. Moreover, in most cases, the propagation velocities for the solitons are different from zero and are of the order of the velocity of the fast mode and/or proton thermal speed. Therefore, the observed magnetic solitons cannot be explained by the mirror instability.

Shock. Another example of compressive coherent structures is shown in Figure 7. The panels are the same as those in Figure 5. Here, we observe an abrupt decrease of the magnetic field modulus $|B|$ (panel (a)). The four satellites observe nearly the same relative amplitude decrease, except the satellite C3, which observed a smaller amplitude gradient. The principal fluctuation δb_z is nearly the same on the four satellites, with small differences. This decrease looks like a shock wave. So, it is expected to be a planar structure. However, differences in the amplitudes of magnetic components on four satellites indicate that the shock front is not perfectly planar, but it probably has ripples or it undergoes a reformation process, e.g., Krasnoselskikh et al. (2013).

Here, the plasma beta is $\beta_p \simeq 1.6$ and the ion temperature anisotropy is $A \simeq 2.1$ on both sides of the decrease. Particle measurements on *Cluster* have a four-second time resolution and so there are only one to two points of measurement within the event. Indeed, sometimes it is possible to use the satellite potential fluctuations (with five measurements per second time resolution) as a proxy of the electron density n_e (Pedersen 1995; Pedersen et al. 2001; Bale et al. 2003). However, this method can give information about n_e in the range 10^{-2} – 10 cm $^{-3}$ (Gustafsson et al. 1997). In our case, the mean plasma density is about 25–30 cm $^{-3}$. Therefore, this method cannot be applied for this particular time interval.

The normal of the structure is quasi-perpendicular to \mathbf{b}_0 ($\Theta_{nB} = 83^\circ \pm 6^\circ$) and it is almost aligned with \mathbf{v}_0 ($\Theta_{nV_\perp} = 15^\circ \pm 11^\circ$), as observed in panels (d) and (e). Therefore, the plane of the structure contains \mathbf{b}_0 and it is perpendicular to \mathbf{v}_0 (see panel (e)). Moreover, the current density, \mathbf{J} , shown in panel (c), is almost perpendicular to \mathbf{b}_0 .

The velocity of propagation in the plasma frame is $\mathcal{V}_0 = -(172 \pm 41)$ km s $^{-1}$. This corresponds to Mach numbers $M_F = \mathcal{V}_0/V_F = (2.8 \pm 1.2)$ and $M_A = \mathcal{V}_0/V_A = (4.9 \pm 1.3)$.

A conclusive interpretation of this structure is difficult without high-resolution density and temperature measurements. However, its strongly compressive nature ($\xi_\parallel = 0.95$) and high values of Mach numbers are compatible with the fast magnetosonic shock wave. Among 109 events, we have found only 3 examples of such shock waves.

3.2.2. Alfvénic Structures

Together with compressive structures (such as holes, solitons, and shocks), we have also detected Alfvénic structures ($\delta b_\perp > \delta b_\parallel$), which have localized, more or less pronounced, compressive fluctuations.

Current sheet. The first example of an Alfvénic structure is shown in Figure 8 (the format of the figure is the same as for the previous examples). Here, the principal variation of the magnetic field is δb_y ; δb_x also has regular variation but with small amplitude, while $\delta b_z \simeq 0$ (see panel (b)). The 3 components reduce (almost) to zero in the center of the structure, where the large-scale magnetic field has its local minimum (panel (a)). This is a property of a current sheet. \mathbf{J} is essentially parallel to \mathbf{b}_0 (panel (c)). The normal to the current sheet \mathbf{n} is perpendicular to \mathbf{b}_0 , and it is oblique to the V_{sw} , $\Theta_{nV_\perp} = 25^\circ \pm 14^\circ$ (panels (d) and (e)). Its thickness, estimated from the four-satellite analysis (see Section 4.2.1 for more details), is $\sim 9\rho_p$. The four satellites observe the same amplitudes of the fluctuations (see panel (b)), which is consistent with the planar geometry. The velocity of this structure in the plasma frame is $\mathcal{V}_0 = (24 \pm 88)$ km s $^{-1}$. Therefore, it is convected by the flow, as expected for a current sheet. It is observed for $\beta_p \simeq 1$ and anisotropy $A \simeq 0.6$. In the subset of 109 structures, 9 examples of current sheets are found, characterized by $\beta_p \lesssim 1$ and $T_\parallel > T_\perp$. Different characteristic sizes are found, from $\sim 4\rho_p$ to $\sim 11\rho_p$.

Vortex structures. Finally, Figures 9–11 show three examples of coherent structures, which look like vortices. They are characterized by a local increase of the background magnetic field, observed by the four satellites (panels (a)). The principal spatial gradients are $\nabla_\perp \gg \nabla_\parallel$, as shown by the timing analysis, for the structures in Figures 10 and 11, which gives $\mathbf{n} \perp \mathbf{b}_0$ (see panels (d) and (e) of Figure 10 and panels (e) and (f) of Figure 11).

In the first two cases, Figures 9 and 10, the principal variations of $\delta \mathbf{b}$ are almost in the plane perpendicular to \mathbf{b}_0 ($\xi_\parallel = 0.16$ and 0.33, respectively) and the current density, \mathbf{J} , displayed in panels (c), is along \mathbf{b}_0 , as in the case of an Alfvén vortex (Petviashvili & Pokhotelov 1992; Alexandrova 2008). The variations of the magnetic magnitude and components from one satellite to another are similar to what is observed for dipolar Alfvén vortices in the Earth’s magnetosheath (Alexandrova et al. 2006) and compatible with a cylindrical structure, crossed by the four satellites along different paths.

Unfortunately, for the Alfvénic vortex in Figure 9, which is more isolated than the other, the assumptions of the timing method are not verified; therefore, the normal and the velocity of this structure cannot be properly determined. Otherwise, we have an indication about the direction and the velocity of propagation for the other example of an Alfvénic vortex (Figure 10). For this structure, the velocity of propagation along the normal and in the plasma rest frame is

$\mathcal{V}_0 = -(95 \pm 35) \text{ km s}^{-1}$ with $\Theta_{nV_\perp} = 30^\circ \pm 10^\circ$ and the spatial scale is about $\sim 4\rho_p$. To compare with the model of an Alfvén vortex (Petviashvili & Pokhotelov 1992; Alexandrova 2008), it is useful to also evaluate its diameter. This can be estimated as the spatial scale corresponding to $\Delta\tau'$ (see Section 4.2.1), which is about $\sim 8\rho_p$. In terms of plasma parameters, this vortex is observed for $\beta_p \simeq 1.3$ and an isotropic ion distribution.

We observe 12 Alfvén vortices ($\xi_{\parallel} < 0.35$) in the subset of 109 structures. All of them are characterized by propagation speeds different from zero (but smaller than V_A in the limits of the errors) and are observed in plasma regions with β_p of the order of one and isotropic ions. Different characteristic spatial sizes are found, from $\sim 2\rho_p$ to $\sim 8\rho_p$, and typical diameters between $\sim 5\rho_p$ and $\sim 17\rho_p$.

Figure 11 shows an example of the most common coherent event found in our time interval. Panel (b) shows the magnetic fluctuations δb_i in the minimum variance frame (direction of maximum variation in green, intermediate in red and minimum in black). One observes that $\delta b_{\max} \gg \delta b_{\text{int}} \sim \delta b_{\min}$, meaning that the minimum variance direction is not well defined. The direction of the maximum variance is quasi-perpendicular to \mathbf{b}_0 ($\theta_{\max} \simeq 80^\circ$) and the intermediate is almost parallel to \mathbf{b}_0 ($\theta_{\text{int}} \simeq 16^\circ$). Panel (c) displays the same magnetic fluctuations δb_i , but in the BV-frame. This representation shows important fluctuations in the three components of $\delta \mathbf{b}$, with a significant compressive component ($\xi_{\parallel} = 0.5$). We have also an impression that δb_z (blue lines) is a bit more localized (within 0.8 s) than the transversal part (within 2 s). Moreover, for the observed structure, the current density, displayed in panel (d) of Figure 11, is along \mathbf{b}_0 . The velocity of propagation in the plasma frame is $\mathcal{V}_0 = -(158 \pm 27) \text{ km s}^{-1}$ with $\Theta_{nV_\perp} = 16^\circ \pm 7^\circ$. The spatial scale is about $\sim 3\rho_p$, while the diameter is larger than $\Delta\tau'$; in particular it is of the order of $1.5\Delta\tau'$, i.e., of the order of $\sim 10\rho_p$. This vortex is observed for $\beta_p \simeq 0.5$ and an isotropic ion distribution.

At the moment there are no models to describe this kind of fluctuations, but some interpretations will be discussed in Section 5. We will call them compressive vortex-like structures.

In the subset of 109 structures, there are 40 compressive vortices, for which the compressibility parameter varies in the range $\xi_{\parallel} \in [0.35, 1.1]$. Such structures are observed under different plasma conditions: $\beta_p \in [0.3, 3]$ and both parallel and perpendicular temperature anisotropy. Moreover, they can propagate in the flow or can be convected by the wind. Their spatial scales vary between $\sim 1.5\rho_p$ and $\sim 18\rho_p$, while the diameters vary between $\sim 4.5\rho_p$ and $\sim 32\rho_p$.

4. STATISTICAL STUDY OF COHERENT STRUCTURES

In this section we will present, first, the results of the minimum variance analysis (Sonnerup & Scheible 1998) applied to all the detected intermittent structures (~ 600) on C1. Then, we analyze the detected structures using four *Cluster* satellites in order to estimate the normal of the structures and their velocities in the plasma rest frame. This analysis was possible only for 109 events from 600.

4.1. Minimum Variance Analysis of 600 Events

The variance matrix (Sonnerup & Scheible 1998) was calculated for each of the detected intermittent events during

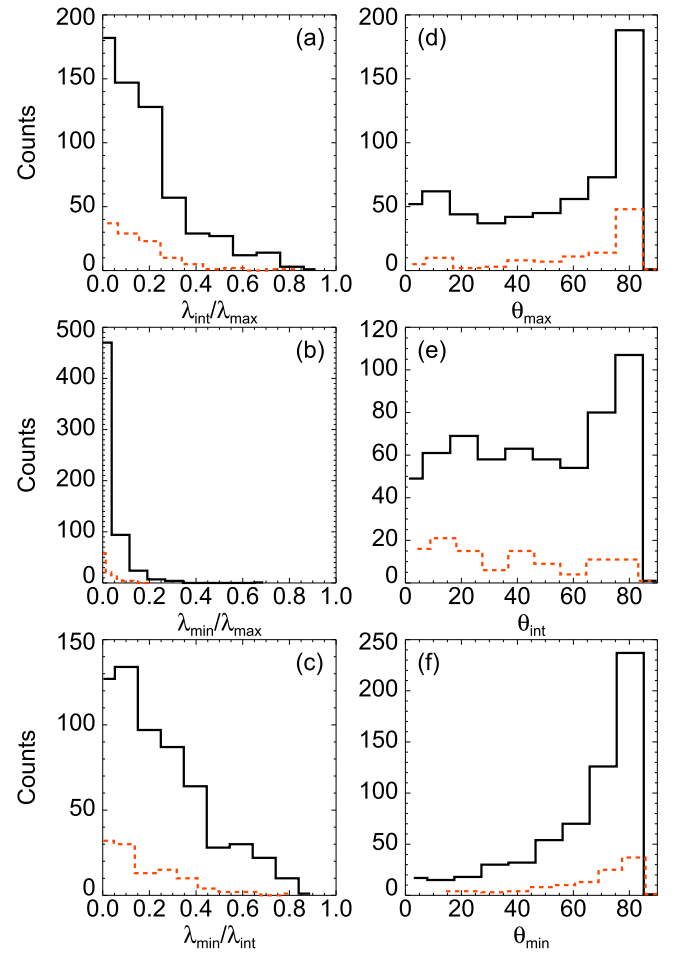


Figure 12. Statistical analysis of the observed coherent structures in the variance frame: 600 selected coherent structures (black) and 109 coherent structures studied using the multi-satellite analysis (red). Left panels: histograms for the intermediate (a) and minimum (b) eigenvalues, normalized to the maximum eigenvalue and for $\lambda_{\min}/\lambda_{\text{int}}$ (c). Right panels: histograms of the angles between the maximum (d), intermediate (e), and minimum (f) variance directions and the local magnetic field.

the time interval of $\Delta\tau'$ around each midpoint of the event (we recall that the temporal widths of the structures are $\Delta\tau' \in [0.75, 7.5] \text{ s}$). Figure 12 shows the results of this analysis: histograms in black display the results for all the events, while the dashed red histograms represent the same results but for the structures that were possible to be studied with four satellites (see Section 4.2.1).

The left column shows normalized values of the eigenvalues of the variance matrix: intermediate λ_{int} and minimal λ_{\min} eigenvalues normalized by λ_{\max} in panels (a) and (b); panel (c) shows $\lambda_{\min}/\lambda_{\text{int}}$. Most of the structures have $\lambda_{\max} \gg \lambda_{\text{int}}, \lambda_{\min}$ (i.e., one-dimensional fluctuations); however, some of them have $\lambda_{\max} \geq \lambda_{\text{int}} \geq \lambda_{\min}$ (two-dimensional fluctuations). For most of the events, $\lambda_{\min}/\lambda_{\max} < 0.2$ and $\lambda_{\min}/\lambda_{\text{int}} < 0.4$; meaning that, in general, the minimum variance direction is well defined. However, for some selected events, there is a degeneracy $\lambda_{\text{int}} \sim \lambda_{\min}$.

The right column gives information on the orientation of the eigenvectors with respect to the local mean magnetic field, evaluated in the same interval in which we perform the minimum variance analysis, $\Delta\tau'$: Θ_{\max} (panel (d)) is the angle between the maximal variance direction $\hat{\mathbf{e}}_{\max}$ and \mathbf{b}_0 .

Respectively, we define, with a similar definition, Θ_{int} (e) and Θ_{min} (f). A large number of selected structures have the direction of maximum variation almost in a direction perpendicular to \mathbf{b}_0 ($\theta_{\text{max}} > 65^\circ$), i.e., *Alfvénic* structures. However, a broad distribution of θ_{max} is obtained, including 25% of structures with the direction of maximum variation almost along \mathbf{b}_0 ($\theta_{\text{max}} < 25^\circ$), i.e., *compressive* structures. The distribution of θ_{int} is almost uniform, with a peak at 80° . Finally, the distribution of θ_{min} shows that $\hat{\mathbf{e}}_{\text{min}}$ is almost perpendicular to \mathbf{b}_0 .

In the case of a planar structure, the direction of the minimum variance of the magnetic fluctuations is oriented parallel to the normal (or to the wavevector \mathbf{k}). However, when $\lambda_{\text{min}} \sim \lambda_{\text{int}}$, the use of $\hat{\mathbf{e}}_{\text{min}}$, as a predictor of the normal to the structure, can be erroneous (Sonnerup & Scheible 1998; Knetter et al. 2004). In order to have robust information about the direction of the normal of the coherent structures, we need a multi-satellite analysis.

4.2. Multi-satellite Analysis of 109 Events

A one-satellite study provides the information only at a single point in space and no relation between temporal and spatial scales can be obtained except using the Taylor hypothesis. Thanks to the four spacecraft, it is possible to determine a normal to a locally planar structure, the speed along this normal, and therefore the spatial scale of the structure without using the Taylor hypothesis. This information allows also the determination of the velocity of the structure in the plasma rest frame.

4.2.1. Normal Velocity in the Satellite Frame and Spatial Scale of the Structures

The approach for determining a normal, \mathbf{n} , to the structure and the velocity along this normal, \mathcal{V} , is called the *timing method*. It is based on the time and space separations (Schwartz 1998):

$$\mathbf{D}_{ij} \cdot \frac{\mathbf{n}}{\mathcal{V}} = \Delta t_{ij}, \quad i, j = 1, 2, 3, 4; i \neq j \quad (14)$$

where $\mathbf{D}_{ij} = \mathbf{D}_j - \mathbf{D}_i$ is a separation vector between the satellites C_i and C_j , and $\Delta t_{ij} = t_j - t_i$ is a temporal delay between measurements on these two satellites. The satellite separations are known with an accuracy of $dD = 0.1$ km. The time separations Δt_{ij} can be determined using the cross-correlation function between signals on two satellites, as was done, for example, in Alexandrova et al. (2006):

$$\mathcal{R}_{ij}(\Delta t) = \frac{\langle \delta \mathbf{B}_i(t) \cdot \delta \mathbf{B}_j(t + \Delta t) \rangle}{\sqrt{\langle \delta \mathbf{B}_i^2 \rangle \langle \delta \mathbf{B}_j^2 \rangle}}; \quad (15)$$

here, the angled brackets indicate the time average and Δt is a time lag. The time lag, that corresponds to a maximum of \mathcal{R}_{ij} , gives the time delay between the satellites, Δt_{ij} . An error for Δt_{ij} could be evaluated taking into account the shape of \mathcal{R}_{ij} and the resolution of magnetic field data. In particular, using Taylor's expansion of \mathcal{R}_{ij} around Δt_{ij} , this error, $d\Delta t_{ij}$, can be written as

$$d\Delta t_{ij} = \sqrt{\frac{2}{\mathcal{R}_{ij}''(\Delta t_{ij})} \frac{\Delta B}{B}}, \quad (16)$$

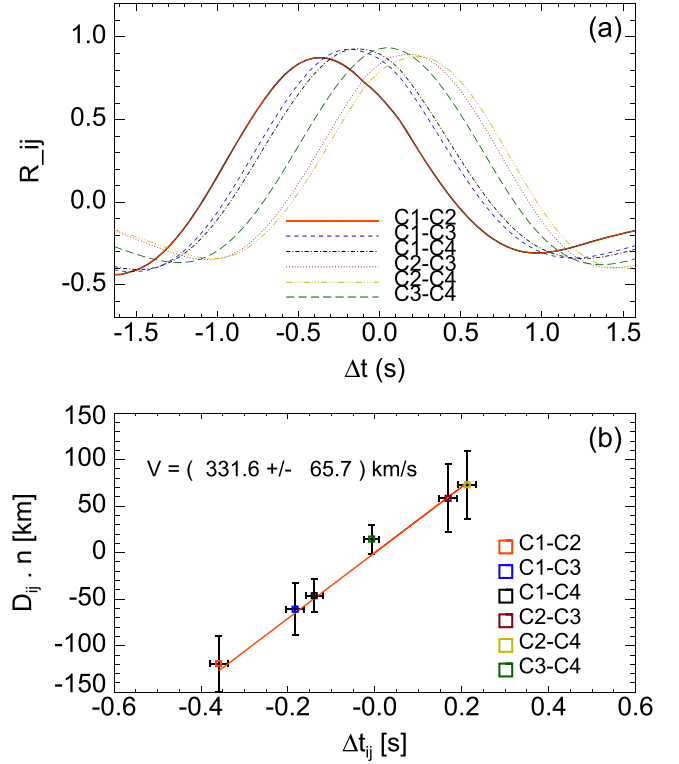


Figure 13. Panel (a): cross-correlation functions, $\mathcal{R}_{ij}(\Delta t)$, for the six satellite pairs for the current sheet, shown in Figure 8, as a function of the time lag. Panel (b): satellite separations along the normal direction as a function of time delays Δt_{ij} between the satellites. The linear fit is indicated by the red solid line.

where \mathcal{R}_{ij}'' is the second derivative of \mathcal{R}_{ij} , evaluated in Δt_{ij} , and $\Delta B/B = 7.813 \times 10^{-3}$ is the relative error for the FGM instrument (Balogh et al. 2001). An example for the determination of the time delays for the current sheet, shown in Figure 8, is given in panel (a) of Figure 13, which shows the six functions $\mathcal{R}_{ij}(\Delta t)$ for the six satellite pairs. The maxima of the functions are well defined and the time lags, corresponding to these maxima, give the time delays, Δt_{ij} .

In order to be sure that all the satellites observe the same structure, the time delays have to satisfy the compatibility relation

$$\Delta t_{ij} = \Delta t_{ik} + \Delta t_{kj}, \quad \Delta t_{ij} = -\Delta t_{ji}. \quad (17)$$

If the compatibility relation is not satisfied, the different satellites most probably do not observe the same event, even if the maximum of \mathcal{R}_{ij} is high (Alexandrova et al. 2006).

Another important assumption of the timing method is the planarity of the structures, moving with constant velocity. These assumptions are somehow related to the compatibility condition, Equation (17). As an example, we report in Figure 13(b) the dependence of separation vectors along the normal direction, $\mathbf{D}_{ij} \cdot \mathbf{n}$, on Δt_{ij} , for the same current-sheet event. The horizontal error for time delays is given by $d\Delta t_{ij}$, while the error on the ordinate axis depends on the errors of the satellite separations and on the normal direction. The red solid line represents the linear fit, whose slope gives an estimation of the constant speed of the structure across four satellites, which in this case is $\mathcal{V} = 331.6 \pm 65.7 \text{ km s}^{-1}$.

Summarizing, the timing method keeps its validity if the following conditions are satisfied: (i) the four satellites observe

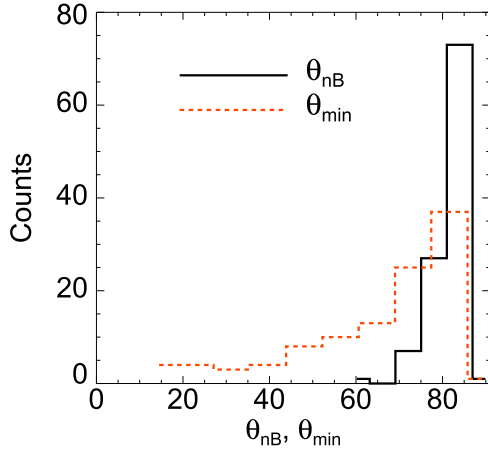


Figure 14. Distribution of the angle between the normal of the structures and the local mean magnetic field, θ_{nB} , in black solid line. The distribution of the angle θ_{\min} between \mathbf{e}_{\min} and \mathbf{b}_0 (red dashed line) is given for comparison.

the same event; (ii) the compatibility relation (Equation (17)) for the time delays is satisfied for all triplets of satellites (that is, verified for the locally planar structures propagating with a constant speed); (iii) the maxima of the cross-correlation function \mathcal{R}_{ij} (Equation (15)), and the corresponding time delays are well defined.

In order to fulfill the conditions listed above, for each structure, we verify that (1) the time error on the compatibility relation is small: $|\Delta t_{ij} - \Delta t_{ik} - \Delta t_{kj}| < 3\delta t$, $\delta t = 0.045$ s being the time resolution of the FGM instrument; (2) there are no zero values in the time separation vector Δt_{ij} ; (3) the relative error on \mathcal{V} is less than 20%; (4) the difference between \mathcal{V} , determined by the timing method, and from the linear fitting in the plane ($\mathbf{D}_{ij} \cdot \mathbf{n}$, Δt_{ij}), as shown in Figure 13(b), \mathcal{V}_{fit} , is less than twice the minimum of the errors on \mathcal{V} and \mathcal{V}_{fit} , i.e., $|\mathcal{V}_{\text{fit}} - \mathcal{V}| < 2 \cdot \min(d\mathcal{V}_{\text{fit}}, d\mathcal{V})$.⁶ The four conditions are simultaneously verified by 109 structures from 600, and only for these events we are confident that we are able to determine properly \mathbf{n} and \mathcal{V} via the multi-satellite analysis.

The red histograms in Figure 12 correspond to the 109 structures, for which \mathbf{n} and \mathcal{V} can be estimated. These red histograms look like the corresponding black ones (for the total number of structures). This means that the 109 structures belong to a representative subfamily of the 600 selected structures. In the following part of the paper, only the results for these 109 structures are shown.

Figure 14 shows the angle between \mathbf{n} and \mathbf{b}_0 , θ_{nB} (black solid histogram), compared with θ_{\min} (red dashed histogram). Even if the distribution of θ_{\min} has its maximum around $\sim 80^\circ$, it also covers small angles. The results of the timing show that θ_{nB} is always close to $\sim 90^\circ$, without cases with small angles, i.e., all magnetic coherent structures have $k_\perp \gg k_\parallel$, a wave-vector anisotropy. The discrepancy between the directions of \mathbf{e}_{\min} and \mathbf{n} comes from the fact that \mathbf{e}_{\min} is not well defined for magnetic structures with $\lambda_{\text{int}} \simeq \lambda_{\text{min}}$. This comparison between θ_{nB} and θ_{\min} shows that the four-satellite analysis is much more robust

⁶ $d\mathcal{V}_{\text{fit}}$ is the 1-sigma fitting error in slope and intercept for \mathcal{V}_{fit} , while $d\mathcal{V}$ is obtained from the propagation of the errors for Equation (14):

$$d\mathcal{V} = \mathcal{V} \left(\frac{\langle d\Delta t_{ij} \rangle}{\max(|\Delta t_{ij}|)} + \frac{dD}{\max(D_{ij})} + dn \right), \quad (18)$$

where dn is the error on the normal determination (see details in Section 4.2.2).

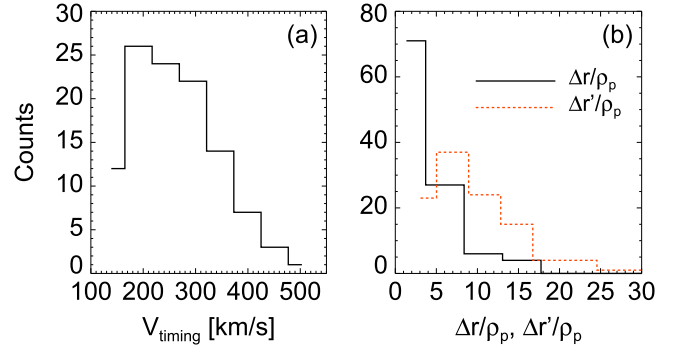


Figure 15. Panel (a): distribution of the velocity along the normal, \mathcal{V} , in the satellite frame. Panel (b): distributions of the spatial scale, Δr (black solid line), and of the total extension, $\Delta r'$ (red dashed line), normalized by ρ_p .

in the determination of the normal for the structures, especially for events with $\delta b_{\text{max}} \gg \delta b_{\text{int}} \sim \delta b_{\text{min}}$.

The velocity along the normal of the structures is $\mathcal{V} \in [150, 500]$ km s⁻¹; see Figure 15(a). Using this information, we estimate along the normal the spatial scale, Δr , and the total extension, $\Delta r'$, of the structures:

$$\Delta r = \mathcal{V} \Delta \tau \quad \text{and} \quad \Delta r' = \mathcal{V} \Delta \tau', \quad (19)$$

$\Delta \tau$ and $\Delta \tau'$ being the timescale and the width of each structure, respectively, as defined above (see Section 3.1). Figure 15(b) shows the distributions of Δr (black solid line) and $\Delta r'$ (red dashed line) normalized by ρ_p , with the proton Larmor radius estimated locally inside each structure. The typical scales of the analyzed structures are around $(2-8)\rho_p$, while the total extensions are around $(3-13)\rho_p$. By taking into account the normalization with the ion inertial length, λ_p (not shown here), the behavior does not change, but the distributions are more peaked and in particular $\Delta r/\lambda_p$ is around 2 and 5, while $\Delta r'/\lambda_p$ is around 5 and 12.

4.2.2. Velocity of the Structures in the Plasma Frame

Once \mathcal{V} has been estimated by multi-point measurements, it is possible to determine for each coherent event the velocity component along the normal direction, \mathcal{V}_0 , in the plasma frame:

$$\mathcal{V}_0 = \mathcal{V} - \mathbf{v}_{\text{sw}} \cdot \mathbf{n}, \quad (20)$$

where \mathbf{v}_{sw} is the local mean speed of the solar wind. The absolute error on \mathcal{V}_0 is

$$d\mathcal{V}_0 = d\mathcal{V} + dv_{\text{sw}} \cos \theta_{nV} + v_{\text{sw}} \sin \theta_{nV} d\theta_{nV}, \quad (21)$$

where $d\mathcal{V}$ is the error on \mathcal{V} , as defined above; dv_{sw} is the error for the CIS/HIA solar wind velocity measurements (about 5% of the bulk velocity; Paschmann et al. 1998); the error $d\theta_{nV}$ includes the angular error for the solar wind velocity vector, which is $\sim 5^\circ$ (Rème et al. 1997), and the error on the normal determination (see Section 4.6 in Vogt et al. 2008). The angular error of \mathbf{n} is different for each structure. It has a distribution cone of uncertainty that peaks around 5° , with minimum and maximum values of about 1.5° and 18° , respectively.

Figure 16(a) shows the results of the calculations of \mathcal{V}_0 for the 109 structures with the corresponding error bars. The structures are ordered by increasing \mathcal{V}_0 . Although the majority of the structures (about 75%) can be considered, within the limit of the errors, convected by the wind, the remaining part of

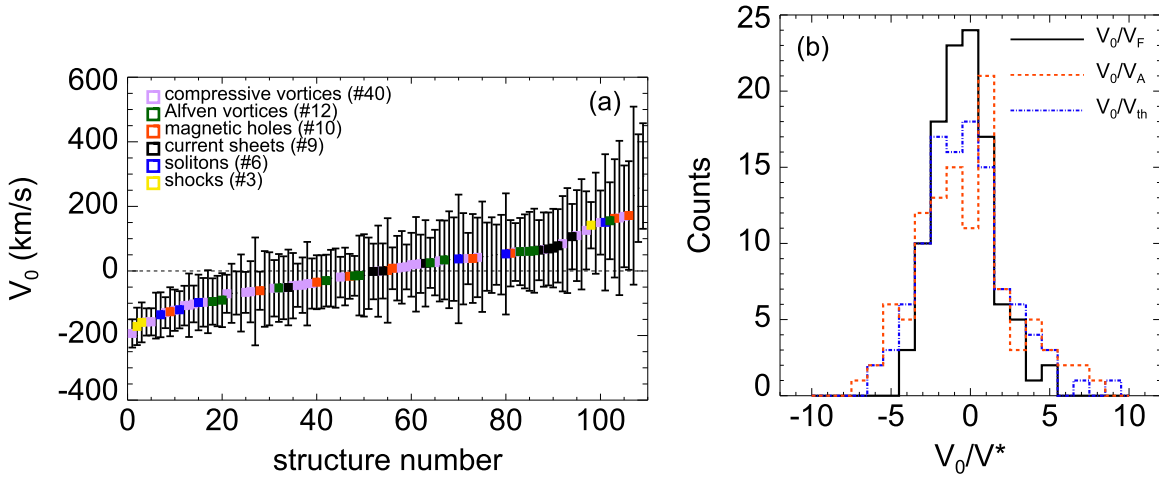


Figure 16. Panel (a): velocity of 109 structures in the plasma frame V_0 , with the corresponding error bars and arranged in increasing order of V_0 . The different families of the structures are indicated by different colors. The number of the structures, for each family, is indicated in the legend. Panel (b): distribution of V_0 normalized by fast magnetosonic speed, V_F (black solid line), Alfvén speed, V_A (red dashed line) and proton thermal speed, V_{th} (blue dash-dot line).

the structures possesses significant velocities different from zero. In general, the nature of the different structures does not display any correlation with the value of V_0 . We have found that magnetic holes (red) and solitons (blue), but also the two kinds of vortices (compressive in lilac and Alfvénic in green), can propagate with $|V_0| > 0$ or be convected by the wind ($V_0 \simeq 0$). Although almost all the current sheets (black) are convected, two examples of these structures have the velocity V_0 different from zero. On the other hand, the three examples of shocks (yellow) have clear velocities much greater than zero.

Figure 16(b) displays the distribution of V_0 , normalized by the speed for the fast modes V_F (black histogram), by the Alfvén speed V_A (red dashed line), and by the proton thermal speed V_{th} (blue dash-dot line). The characteristic velocities are calculated in the upstream region for each structure, which is known from the sign of V_0 . The narrowest distribution, which seems to be the most suitable, is found for the histogram of V_0/V_F , showing that most of the structures propagates within $[-3, 2]V_F$ limits. But, as discussed above, these limits are due to the error bars on V_0 , i.e., the structures from the central part of the histogram are, most probably, just convected by the wind.

As one can see from Figure 16(a) the errors dV_0 can be very large. A rough estimate of dV_0 (Equation (21)) shows that, even though dV is small, the other two terms can be large. These last terms are sensitive to the value of θ_{nV} (angle between the normal of the structure and the local solar wind speed). The two limit cases for θ_{nV} are (i) $\theta_{nV} \simeq 0^\circ$, which means $dV_0 = dV + dv_{sw} \sim V_A$; and (ii) $\theta_{nV} \simeq 90^\circ$, which gives $dV_0 \sim dV + v_{sw}d\theta_{nV} \sim 1.3V_A$ or $\sim 4V_A$ (for the limit cases of $d\theta_{nV} = 6.5^\circ$ and 23° , respectively). All the other cases are a combination of different contributions. The dependence of dV_0 on θ_{nV} for all 109 structures is shown in Figure 17: higher values of dV_0 are observed for higher values of θ_{nV} . The different classes of structures are indicated by different colors (see legend). The structures whose nature is not clear are presented in gray.

5. CONCLUSIONS AND DISCUSSIONS

In this paper, motivated by an increase of magnetic compressibility around ion characteristic scales, we have

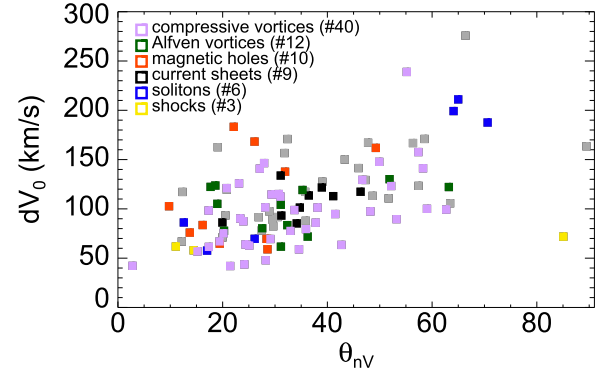


Figure 17. Error dV_0 (see Equation (21)) as a function of the angle between the normal to the structure and the local solar wind velocity, θ_{nV} , for the 109 structures, separated in different classes (different colors). The number of structures, for each different nature, is also indicated in the legend.

studied compressive coherent structures in a slow solar wind stream in the frequency range [0.1, 2] Hz. The analyzed stream is characterized by a plasma beta that varies over a decade between 0.3 and 5.

Different families of structures have been detected. Among strongly compressive events with $\delta b_{\parallel} \gg \delta b_{\perp}$ we find (1) magnetic solitons, (2) magnetic holes, and (3) shock waves. Examples of Alfvénic structures, i.e., with $\delta b_{\perp} > \delta b_{\parallel}$, are (1) current sheets and (2) vortex-like structures, which can be Alfvénic with $\delta b_{\perp} \gg \delta b_{\parallel}$, but also with $\delta b_{\perp} \gtrsim \delta b_{\parallel}$. In this interval of slow solar wind, we have found that the most frequent class of coherent structures are the vortex-like structures and in particular the structures that we have named here compressive vortices.

Thanks to a multi-satellite analysis, we have determined normals \mathbf{n} to the structures, and the velocity along \mathbf{n} . Independently of the nature of the structures, \mathbf{n} is always perpendicular to \mathbf{b}_0 . This means that the strongest gradients are in the plane perpendicular to \mathbf{b}_0 , i.e., $k_{\perp} \gg k_{\parallel}$. Characteristic spatial scales of the structures along \mathbf{n} vary between 2 and 20 ρ_i and λ_i .

The topology of the observed coherent structures can be (i) a quasi-planar isolated front (compatible with soliton, shock, current sheet) with the mean magnetic field in the plane of the

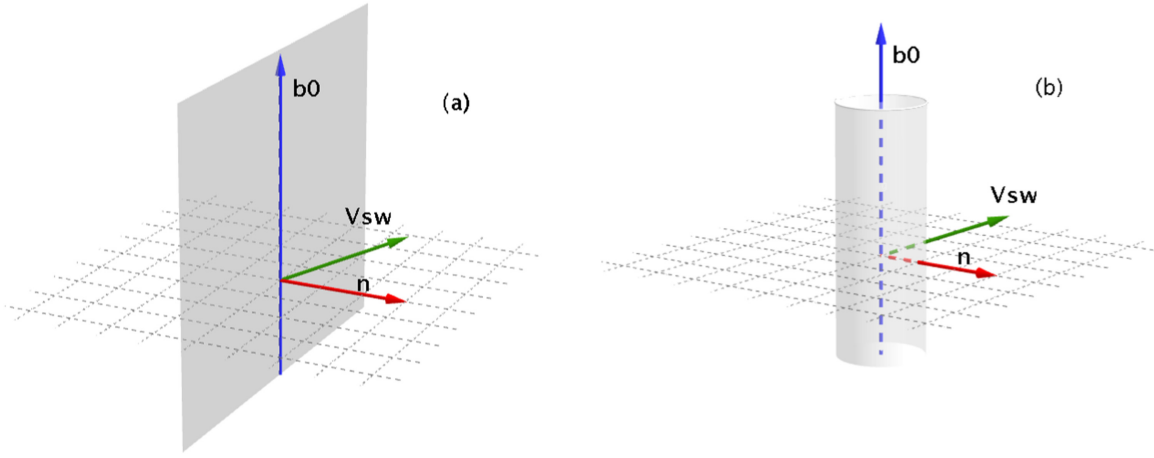


Figure 18. Two-dimensional (a) and three-dimensional (b) geometry models for the structures. The normal of the structures is indicated by the red arrow; the velocity of the flow is represented by the green arrow, while the local magnetic field is in blue.

front (see Figure 18(a)); or (ii) a cylinder, or a cigar, with the axis along the local mean magnetic field and the normal parallel to the radius of the cylinder (see Figure 18(b)). This last topology is compatible with the magnetic holes and vortices. To confirm the geometry of the structures, a comparison of the signals on the four satellites with different models for different structures should be done (that will be a subject of our future work).

Our multi-satellite analysis shows that the velocity of the structures along \mathbf{n} in the plasma rest frame is zero (within the error bars) for 75% of the structures that we could study with four satellites. The remaining 25% of the structures manifests significant velocities different from zero and may take values of several V_F (fast magnetosonic speed). However, we point out that the errors on the estimated velocities can be huge, meaning that in the limit of these errors the velocities could be lower, but not zero.

The statistical study of all structures does not show any dependences between properties of the structures (size, amplitude, speed) and the plasma parameters. However, considering them by types, we realize the following.

1. Compressive vortices (40 examples of 109; see Figure 11) are the most frequently observed structures, characterized by $\langle \delta b/B_0 \rangle \sim 0.1$ and $\xi_{\parallel} > 0.35$ (see Equation (13)). They can be found in the plasma region with both $\beta_p < 1$ and $\beta_p > 1$ ($\langle \beta_p \rangle \sim 1.5$) and for both $T_{\parallel} > T_{\perp}$ and $T_{\parallel} < T_{\perp}$ (proton temperature anisotropy $\langle A \rangle \sim 1.1$). The compressive vortices can propagate with $|\mathcal{V}_0| \in [1, 4] V_A$ or be convected by the flow. Their size varies between $\sim 1.5 \rho_p$ and $\sim 18 \rho_p$, while the diameters between $\sim 4.5 \rho_p$ and $\sim 32 \rho_p$.
2. Alfvén vortex-like structures (12 examples of 109; see Figures 9 and 10) have $\langle \delta b/B_0 \rangle \sim 0.1$ and $\xi_{\parallel} < 0.35$. They are observed for $\langle \beta_p \rangle \sim 1.2$ and isotropic ions. The characteristic propagation speeds $|\mathcal{V}_0| \in [0.5, 2] V_A$. Different sizes are also found: from $\sim 2 \rho_p$ to $\sim 8 \rho_p$ and typical diameters between $\sim 5 \rho_p$ and $\sim 17 \rho_p$.
3. Magnetic holes (10 examples of 109; see Figures 5 and 6) usually have amplitudes $\langle \delta b/B_0 \rangle \sim 0.06$ and $\langle \xi_{\parallel} \rangle \sim 1.7$, with current density strictly perpendicular to the local magnetic field. They appear in high beta plasma ($\langle \beta_p \rangle \sim 2$), and $T_{\perp} > T_{\parallel}$ ($\langle T_{\perp}/T_{\parallel} \rangle \sim 1.5$). They are

usually convected by the flow in the limits of errors. Typical size $\Delta r \in [2, 10] \rho_p$.

4. Current sheets (9 examples of 109; see Figure 8) have strong amplitudes $\langle \delta b/B_0 \rangle \sim 0.25$ and are convected by the flow. The plasma parameters are characterized by values of $\beta_p \lesssim 1$ and $T_{\parallel} > T_{\perp}$. The sizes for the current sheets vary between $\sim 4 \rho_p$ and $\sim 11 \rho_p$.
5. Solitons (6 examples of 109; see Figure 4) have small amplitudes ($\langle \delta b/B_0 \rangle \sim 0.05$) and they are strongly compressive ($\langle \xi_{\parallel} \rangle \sim 1.7$). They are observed for a moderate ion beta ($\langle \beta_p \rangle \sim 1.2$) and almost isotropic ion distributions ($\langle T_{\perp}/T_{\parallel} \rangle \sim 1.2$). These structures propagate with the typical velocity of the fast modes, V_F , and have characteristic sizes of ~ 5 – $6 \rho_p$ and λ_p .
6. Shocks (3 examples of 109; see Figure 7) have an amplitude of $\langle \delta b/B_0 \rangle \sim 0.05$ and propagate fast in the flow. The first example has $\mathcal{V}_0 = (142 \pm 64) \text{ km s}^{-1}$, Mach numbers $M_F = 2.7$ and $M_A = 4.5$, size of $\sim 7 \rho_p$, and it is observed for $\beta_p \sim 1$ and $T_{\parallel} > T_{\perp}$ ($A \simeq 0.6$), while the second one (see Figure 7) has $\mathcal{V}_0 = -(172 \pm 58) \text{ km s}^{-1}$, Mach numbers $M_F = 2.8$ and $M_A = 4.9$, size of $\sim 4 \rho_p$, and it is found for $\beta_p > 1$ and $A > 1$. The third example has almost the same characteristic of the shock in Figure 7; in particular $\mathcal{V}_0 = -(160 \pm 51) \text{ km s}^{-1}$, $M_F = 2.6$, $M_A = 4.3$, and typical size of $\sim 4 \rho_p$. Moreover, this example of shock is also found for $\beta_p > 1$ and $A > 1$.

In incompressible MHD theory, one expects to find current sheets and elongated structures, related to the intermittency of the magnetic field (Carbone et al. 1990). Recently, Servidio et al. (2014b) have shown the existence, in the solar wind, of these equilibria, predicted by the MHD relaxation theory, which spontaneously emerge during the turbulent cascade.

Most of the studies of plasma discontinuities are based on the use of the PVI technique (Greco et al. 2008) or Haar wavelet (Veltri & Mangeney 1999). These methods are oriented to catch planar/slab discontinuities in different regimes of the turbulence cascade. Around ion scales (as in the case of the present work), these studies, applied to both solar wind in situ measurements and numerical simulations, reveal mostly the presence of current sheets (Greco et al. 2012b; Greco & Perri 2014). Therefore, coherent current sheets were considered as the principal cause of intermittency in space

plasma at ion scales. Here, we have shown for the first time that in the case of the slow solar wind, very different types of coherent structures contribute to the intermittency at proton scales and current sheets are not the most common ones. In our study, we observe only $\sim 10\%$ of coherent structures in the form of current sheets and another $\sim 10\%$ in the form of Alfvénic vortices. Otherwise, a considerable part of the structures are compressive vortices ($\sim 35\%$), magnetic holes, solitons, and shocks ($\sim 20\%$ in total). The remaining 25% of the 109 structures are not well identified because of the interaction of adjacent structures with the selected intermittent events.

It is important to point out that the dominance of coherent structures in the form of vortices is not due to the choice of thresholding fluctuations of the parallel component of the magnetic field. In fact, by performing the same analysis in this interval of slow solar wind, but with a threshold on the total magnetic energy, preliminary results show that the nature of the most frequent structures does not change. In 140 observed structures, for which only 40% are well identified, the most common structures remain vortices ($\sim 26\%$) and not current sheets ($\sim 11\%$). The main difference between the two analyses is that, in the case of total magnetic fluctuations, the level of the energy threshold is higher with respect to the compressive one. Therefore, in this case, the majority of compressive structures disappears, due to their low energetic nature, and only a few examples of magnetic holes and solitons are recognized ($\sim 2\%$). Moreover, the dominant class of vortices in this case are Alfvénic ($\sim 80\%$ of the total structures in the form of vortices).

Otherwise, different results are obtained if a stream of fast solar wind is considered (for example the same interval used in Leamon et al. 1998 and Lion et al. 2016). In this stream of fast solar wind observed by the *Wind* spacecraft, even if we consider thresholding compressive fluctuations, no compressive structures are found. For 254 structures detected around ion characteristic scales, we have been able to identify 30% of them well, for which the nature of magnetic fluctuations appears to be characterized by the presence of coherent structures in the form of vortices ($\sim 17\%$, including $\sim 87\%$ of Alfvénic vortices) and current sheets ($\sim 13\%$). Examples of wave packets are also found ($\sim 8\%$). In conclusion, it seems that the presence of compressive structures are especially related to the characteristic velocity of the solar wind stream. For the future, we will study several intervals of solar wind data with different properties to have a general description of magnetic fluctuations around ion scales.

In the present paper, the most frequent structures (the so called compressive vortices) are characterized by the component of maximum variance almost perpendicular to \mathbf{b}_0 and the intermediate component almost parallel to \mathbf{b}_0 . Moreover, the compressive component (as shown in panel (c) of Figure 11) is a bit more localized within the structure, while the Alfvénic part is more delocalized, extending itself outside $\Delta\tau'$. This kind of structure could be described by the preliminary results of a hydrodynamic model of coherent vortices, in warm plasma ($\beta_p \sim \beta_e \sim 1$), with perpendicular spatial scales comparable to the ion characteristic scales. These preliminary results indicate that the Larichev–Reznik type of coherent dipolar structures (Larichev & Reznik 1976) may also appear in a high β plasma. They are characterized by a very small parallel electric field and by a localized compressional component of the magnetic field in the interior of the vortex core, while the torsional components can have larger spatial extent outside the

core edge. This work is in progress and the results will be published elsewhere (D. Jovanovic et al. 2016, in preparation).

On the other hand, another possible explanation for these compressive vortices could be to consider them as a non-linear evolution of KAW. Recent observational (Sahraoui et al. 2010; Salem et al. 2012; Podesta 2013; Roberts et al. 2013, 2015) and numerical studies (Vásconez et al. 2015) have shown that the ion characteristic scales in turbulent solar wind plasma are characterized by the presence of fluctuations with properties of KAWs (like k-anisotropy and compressibility). These waves belong to the Alfvén branch, with wavelength comparable to the proton inertial length/Larmor radius and wave vectors nearly perpendicular to the mean magnetic field. KAW are also characterized by compressive (parallel) magnetic field fluctuations and by a parallel electric field component (Lee et al. 1994). To test this idea, we can evaluate the expected ratio of magnetic compressibility for KAW, as defined in Equation (55) of Boldyrev et al. (2013), inside the detected compressive vortices. The preliminary results show that for compressive vortices with $\xi_{\parallel} \in [0.47, 0.7]$, the ratio of magnetic compressibility is in agreement with the prediction for KAW. On the other hand, when $\xi_{\parallel} < 0.47$ and $\xi_{\parallel} > 0.7$, the prediction is not in agreement with observations. Therefore, no definitive conclusion can be made at this point. A more detailed study to describe these structures should be done and this will be a subject of future work.

The other important contribution in our interval is given by one-dimensional (i.e., linearly polarized) compressive structures, such as magnetic holes and solitons. The detected magnetic holes are characterized by $T_{\perp} > T_{\parallel}$, high values of β_p and velocity in the plasma frame, \mathcal{V}_0 , almost zero in the limits of the errors. These characteristics are in agreement with the properties of the mirror mode structures. During the last decades, the structures in the form of solitary magnetic depression and humps, or a combination of both, observed in the interplanetary medium, have been mainly described as non-linear mirror mode (Soucek et al. 2008; Génot et al. 2009).

In our case, however, we have found that the solitons are not convected by the flow. Therefore, we cannot interpret them as non-linear mirror modes. Recently, Narita & Marsch (2015) proposed a new dissipation mechanism, related to the proton Landau damping of the quasi-perpendicular kinetic slow mode. This mode, linked to the oblique MHD slow mode, has shorter wavelengths going down to the proton inertial length and its phase velocity is the proton thermal speed. Moreover, the kinetic slow mode exhibits a compressive character that is similar to the MHD slow mode (with magnetic field fluctuations nearly aligned with the mean magnetic field). The compressive solitons, described in our paper, propagate perpendicular to the magnetic field with finite velocities in the plasma frame, comparable to the velocity for the fast modes and/or to the proton thermal speed. Unfortunately, due to the errors on the evaluation of the velocity, it is not possible to confirm that the velocity of propagation is exactly the proton thermal speed. However, it could be realistic that the magnetic solitons observed here can be described as a non-linear evolution of the kinetic slow mode.

The quasi-perpendicular kinetic slow mode can also lead to the efficient heating of the protons in the parallel direction by the Landau resonance mechanism and maybe in the perpendicular direction by pitch angle scattering (Narita & Marsch 2015). Due to the low resolution of the particle measurements

on *Cluster* (4 s), there are just one or two points of measurement within an event. Therefore, it is impossible to conclude anything about the heating process at the moment. A more detailed study of our compressive structures is needed and it will be investigated in future works using kinetic simulations.

The understanding of the physical mechanisms that generate coherent structures and how these events contribute to dissipation in collisionless plasma could provide key insights into the general problem of solar wind heating. Recently, solar wind measurements and numerical simulations have shown that a connection between kinetic processes and intermittent turbulence exists. Particle heating and acceleration and temperature anisotropy appear localized in and near coherent structures (Perrone et al. 2013b, 2014b; Wu et al. 2013). This means that the connection between intermittent turbulence, coherent structures, and kinetic effects on particle distribution functions cannot be ignored (Perrone et al. 2013a). However, unfortunately, the existing particle “in situ” measurements have several limitations in temporal, energy, and angular resolutions. In particular, due to low time resolution of particle data, there are not enough measurements within the structures to study the heating processes at kinetic scales and sometimes this low resolution can generate unphysical effects due to the procedure of data sampling and averaging (Perrone et al. 2014a). Moreover, accelerated particles, which appear as a beam in the distribution functions, can be resolved only if the resolution in velocity space is sufficiently high. This means that higher energy and angular resolutions of particle distributions are also crucial. The recent space mission *MMS* has improved the temporal resolution for the particle measurements, but angular/energy resolution still remains insufficient to resolve solar wind ions. An important contribution to studying dissipation mechanisms in the solar wind, with the best measurements in terms of temporal, energy, and angular resolutions for three-dimensional particle distributions, might be provided by the future mission currently under study, *THOR*. Such measurements are required to study the connection between coherent structures and kinetic effects on the particle distribution functions.

All *Cluster* data are obtained from the ESA Cluster Active Archive. We thank the FGM, CIS, WHISPER, and PEACE instrument teams and the ESA Cluster Science Archive. D.P. would like to acknowledge S. Lion, L. Matteini, G. Chanteur, C. Boutillier, and H. Middleton for helpful conversations. The authors would like to acknowledge the anonymous referee for comments that greatly helped to improve the manuscript.

REFERENCES

- Alexandrova, O. 2008, *NPGeo*, **15**, 95
- Alexandrova, O., Carbone, V., Veltri, P., & Sorriso-Valvo, L. 2007, *P&SS*, **55**, 2224
- Alexandrova, O., Carbone, V., Veltri, P., & Sorriso-Valvo, L. 2008, *ApJ*, **674**, 1153
- Alexandrova, O., Lacombe, C., Mangeney, A., Grappin, R., & Maksimovic, M. 2012, *ApJ*, **760**, 121
- Alexandrova, O., Mangeney, A., Maksimovic, M., et al. 2004, *JGR*, **109**, A05207
- Alexandrova, O., Mangeney, A., Maksimovic, M., et al. 2006, *JGR*, **111**, A12208
- Alexandrova, O., & Saur, J. 2008, *GeoRL*, **35**, 15102
- Alexandrova, O., Saur, J., Lacombe, C., et al. 2009, *PhRvL*, **103**, 165003
- Bale, S. D., Kellogg, P. J., Mozer, F. S., Horbury, T. S., & Reme, H. 2005, *PhRvL*, **94**, 215002
- Bale, S. D., Mozer, F. S., & Horbury, T. S. 2003, *PhRvL*, **91**, 265004
- Balogh, A., Carr, C. M., Acuña, M. H., et al. 2001, *AnGeo*, **19**, 1207
- Baumgärtel, K. 1999, *JGR*, **104**, 28295
- Biskamp, D. 1993, *Nonlinear Magnetohydrodynamics* (Cambridge: Cambridge Univ. Press)
- Boldyrev, S., Horaites, K., Xia, Q., & Perez, J. C. 2013, *ApJ*, **777**, 41
- Bourouaine, S., Alexandrova, O., Marsch, E., & Maksimovic, M. 2012, *ApJ*, **749**, 102
- Bruno, R., & Carbone, V. 2005, *LRSP*, **2**, 4
- Bruno, R., Carbone, V., Sorriso-Valvo, L., & Bavassano, B. 2003, *JGR*, **108**, 1130
- Bruno, R., Carbone, V., Veltri, P., Pietropaolo, E., & Bavassano, B. 2001, *P&SS*, **49**, 1201
- Bruno, R., D’Amicis, R., Bavassano, B., Carbone, V., & Sorriso-Valvo, L. 2007, *P&SS*, **55**, 2233
- Bruno, R., Trenchi, L., & Telloni, D. 2014, *ApJL*, **793**, L15
- Burlaga, L. F. 1991, *JGR*, **96**, 5847
- Burlaga, L. F. 1993, *JGR*, **98**, 17467
- Carbone, V., Bruno, R., & Veltri, P. 1996, *GeoRL*, **23**, 121
- Carbone, V., Veltri, P., & Bruno, R. 1995, *PhRvL*, **75**, 3110
- Carbone, V., Veltri, P., & Mangeney, A. 1990, *PhFl*, **8**, 1487
- Chasapis, A., Retinò, A., Sahraoui, F., et al. 2015, *ApJL*, **804**, L1
- Décroau, P. M., Fergeau, P., Krasnoselskikh, V., et al. 2001, *AnGeo*, **19**, 1241
- Dunlop, M. W., Balogh, A., Glassmeier, K.-H., & Robert, P. 2002, *JGR*, **107**, 1384
- Dunlop, M. W., Southwood, D. J., Glassmeier, K.-H., & Neubauer, F. M. 1988, *AdSpR*, **8**, 273
- Erdős, G., & Balogh, A. 1996, *JGR*, **101**, 1
- Farge, M. 1992, *AnRFM*, **24**, 395
- Frisch, U. 1995, *Turbulence: The Legacy of A. N. Kolmogorov* (Cambridge: Cambridge Univ. Press)
- Génot, V., Budnik, E., Hellinger, P., et al. 2009, *AnGeo*, **27**, 601
- Gosling, J. T., McComas, D. J., Roberts, D. A., & Skoug, R. M. 2009, *ApJL*, **695**, L213
- Greco, A., Chuychai, P., Matthaeus, W. H., Servidio, S., & Dmitruk, P. 2008, *GeoRL*, **35**, L19111
- Greco, A., Matthaeus, W. H., D’Amicis, R., Servidio, S., & Dmitruk, P. 2012a, *ApJ*, **749**, 105
- Greco, A., & Perri, S. 2014, *ApJ*, **784**, 163
- Greco, A., Valentini, F., Matthaeus, W. H., Servidio, S., & Dmitruk, P. 2012b, *PhRvE*, **86**, 066405
- Gustafsson, G., Bostrom, R., Holback, B., et al. 1997, *SSRv*, **79**, 137
- Hamilton, K., Smith, C. W., Vasquez, B. J., & Leamon, R. L. 2008, *JGR*, **113**, A01106
- Haynes, C. T., Burgess, D., Camporeale, E., & Sundberg, T. 2015, *PhPl*, **22**, 012309
- He, J., Marsch, E., Tu, C., Yao, S., & Tian, H. 2011, *ApJ*, **731**, 85
- He, J., Tu, C., Marsch, E., & Yao, S. 2012, *ApJL*, **745**, L8
- Horbury, T. S., Balogh, A., Forsyth, R. J., & Smith, E. J. 1997, *AdSpR*, **19**, 847
- Kellogg, P. J., & Horbury, T. S. 2005, *AnGeo*, **23**, 3765
- Kiyani, K. H., Chapman, S. C., Sahraoui, F., et al. 2013, *ApJ*, **763**, 10
- Knetter, T., Neubauer, F. M., Horbury, T., & Balogh, A. 2004, *JGR*, **109**, A06102
- Kolmogorov, A. 1941, *DoSSR*, **30**, 301
- Krasnoselskikh, V., Balikhin, M., Walker, S. N., et al. 2013, *SSRv*, **178**, 535
- Lacombe, C., Alexandrova, O., Matteini, L., et al. 2014, *ApJ*, **796**, 5
- Larichev, V. D., & Reznik, G. M. 1976, *Rep. USSR Acad. Sci.*, **231**, 1077
- Leamon, R. J., Matthaeus, W. H., Smith, C. W., et al. 2000, *ApJ*, **537**, 1054
- Leamon, R. J., Smith, C. W., Ness, N. F., Matthaeus, W. H., & Wong, H. K. 1998, *JGR*, **103**, 4775
- Lee, L. C., Johnson, J. R., & Ma, Z. W. 1994, *JGR*, **99**, 17405
- Lion, S., Alexandrova, O., & Zaslavsky, A. 2016, *ApJ*, **824**, 47
- Marsch, E. 2006, *LRSP*, **3**, 1
- Marsch, E., & Tu, C.-Y. 1994, *AnGeo*, **12**, 1127
- Matteini, L., Horbury, T. S., Neugebauer, M., & Goldstein, B. E. 2014, *GeoRL*, **41**, 259
- Matthaeus, W. H., & Goldstein, M. L. 1982, *JGR*, **87**, 6011
- Narita, Y., & Marsch, E. 2015, *ApJ*, **805**, 24
- Newell, A. C., Nazarenko, S. V., & Biven, L. 2001, *PhyD*, **152**, 520
- Osman, K. T., Matthaeus, W. H., Greco, A., & Servidio, S. 2011, *ApJL*, **727**, L11
- Osman, K. T., Matthaeus, W. H., Hnat, B., & Chapman, S. C. 2012, *PhRvL*, **108**, 261103

- Paschmann, G. J., Fazakerley, A. N., & Schwartz, S. J. 1998, *Analysis Methods for Multi-Spacecraft Data* (Noordwijk, The Netherlands: ESA Publ. Div.)
- Pedersen, A. 1995, *AnGeo*, **13**, 118
- Pedersen, A., Décréau, P., Escoubet, C.-P., et al. 2001, *AnGeo*, **19**, 1483
- Perri, S., Goldstein, M. L., Dorelli, J. C., & Sahraoui, F. 2012, *PhRvL*, **109**, 191101
- Perrone, D., Bourouaine, S., Valentini, F., Marsch, E., & Veltri, P. 2014a, *JGR*, **119**, 2400
- Perrone, D., Dendy, R. O., Furno, I., et al. 2013a, *SSRv*, **178**, 233
- Perrone, D., Valentini, F., Servidio, S., Dalena, S., & Veltri, P. 2013b, *ApJ*, **762**, 99
- Perrone, D., Valentini, F., Servidio, S., Dalena, S., & Veltri, P. 2014b, *EPJD*, **68**, 209
- Petviashvili, V. I., & Pokhotelov, O. 1992, *Solitary Waves in Plasmas and in the Atmosphere* (London: Gordon and Breach)
- Pinçon, J.-L., & Lefeuvre, F. 1991, *JGR*, **96**, 1789
- Podesta, J. J. 2013, *SoPh*, **286**, 529
- Podesta, J. J., & Gary, S. P. 2011, *ApJ*, **734**, 15
- Rees, A., Balogh, A., & Horbury, T. S. 2006, *JGR*, **111**, A10106
- Rème, H., Aoustin, C., Bosqued, J. M., et al. 2001, *AnGeo*, **19**, 1303
- Rème, H., Bosqued, J. M., Sauvaud, J. A., et al. 1997, *The Cluster and Phoenix Missions* (Noordwijk: ESA)
- Retinò, A., Sundkvist, D., Vaivads, A., et al. 2007, *NatPh*, **3**, 236
- Roberts, O. W., Li, X., Alexandrova, O., & Li, B. 2016, *JGR*, in press
- Roberts, O. W., Li, X., & Jeska, L. 2015, *ApJ*, **802**, 2
- Roberts, O. W., Li, X., & Li, B. 2013, *ApJ*, **769**, 58
- Sahraoui, F., Goldstein, M. L., Belmont, G., Canu, P., & Rezeau, L. 2010, *PhRvL*, **105**, 131101
- Sahraoui, F., Huang, S. Y., Belmont, G., et al. 2013, *ApJ*, **777**, 15
- Salem, C., Mangeney, A., Bale, S. D., & Veltri, P. 2009, *ApJ*, **702**, 537
- Salem, C. S., Howes, G. G., Sundkvist, D., et al. 2012, *ApJL*, **745**, L9
- Schwartz, S. J. 1998, *Analysis Methods for Multi-Spacecraft Data* (Noordwijk, The Netherlands: ESA Publ. Div.)
- Servidio, S., Gurgiolo, C., Carbone, V., & Goldstein, M. L. 2014b, *ApJL*, **789**, L44
- Servidio, S., Osman, K. T., Valentini, F., et al. 2014a, *ApJL*, **781**, L27
- Servidio, S., Valentini, F., Califano, F., & Veltri, P. 2012, *PhRvL*, **108**, 045001
- She, Z.-S., Jackson, E., & Orszag, S. A. 1990, *Natur*, **344**, 226
- Smith, C. W., Hamilton, K., Vasquez, B. J., & Leamon, R. J. 2006, *ApJL*, **645**, L85
- Sonnerup, B., & Scheible, M. 1998, *Analysis Methods for Multi-Spacecraft Data* (The Netherlands: ESA Publ. Div.)
- Sorriso-Valvo, L., Carbone, V., & Bruno, R. 2005, *SSRv*, **121**, 49
- Sorriso-Valvo, L., Carbone, V., Giuliani, P., et al. 2001, *P&SS*, **49**, 1193
- Soucek, J., Lucek, E., & Dandouras, I. 2008, *JGR*, **113**, A04203
- Stasiewicz, K., Shukla, P. K., Gustafsson, G., et al. 2003, *PhRvL*, **90**, 085002
- Stevens, K. L., & Kasper, J. C. 2007, *JGR*, **112**, A05109
- Sundkvist, S., Krasnoselskikh, V., Shukla, P. K., et al. 2005, *Natur*, **436**, 825
- Sundkvist, S., Retinò, A., Vaivads, A., & Bale, S. D. 2007, *PhRvL*, **99**, 025004
- Szita, S., Fazakerley, A. N., Carter, P. J., et al. 2001, *AnGeo*, **19**, 1721
- Tessein, J. A., Matthaeus, W. H., Wan, M., et al. 2013, *ApJL*, **776**, L8
- Torrence, C., & Combo, G. P. 1998, *BAMS*, **79**, 61
- Tu, C. Y., & Marsch, E. 1995, *SSRv*, **73**, 1
- Turner, J. M., Burlaga, L. F., Ness, N. F., & Lemaire, J. F. 1977, *JGR*, **82**, 1921
- Vásconez, C. L., Pucci, F., Valentini, F., et al. 2015, *ApJ*, **815**, 7
- Veltri, P. 1999, *PPCF*, **41**, A787
- Veltri, P., & Mangeney, A. 1999, in *AIP Conf. Proc.* 471, *Solar Wind IX*, ed. S. Habbal (Melville, NY: AIP), 543
- Verkhoglyadova, O. P., Dasgupta, B., & Tsurutani, B. T. 2003, *NPGEO*, **10**, 335
- Vogt, J., Paschmann, G., & Chanteur, G. 2008, *Multi-Spacecraft Analysis Methods Revisited* (Noordwijk, The Netherlands: ESA Publ. Div.)
- Wan, M., Matthaeus, W. H., Karimabadi, H., et al. 2012a, *PhRvL*, **109**, 195001
- Wan, M., Osman, K. T., Matthaeus, W. H., & Oughton, S. 2012b, *ApJ*, **744**, 171
- Winterhalter, D., Neugebauer, M., Goldstein, B. E., et al. 1994, *JGR*, **99**, 23371
- Wu, P., Perri, S., Osman, K. T., et al. 2013, *ApJL*, **763**, L30
- Zhdankin, V., Boldyrev, S., Mason, J., & Perez, J. C. 2012, *PhRvL*, **108**, 175004